



Airborne observations of peroxy radicals during the EMeRGe campaign in Europe

Midhun George^{1,a}, Maria Dolores Andrés Hernández¹, Vladyslav Nenakhov^{1,b}, Yangzhuoran Liu¹, John Philip Burrows¹, Birger Bohn², Eric Förster³, Florian Obersteiner³, Andreas Zahn³, Theresa Harlaß⁴, Helmut Ziereis⁴, Hans Schlager⁴, Benjamin Schreiner⁵, Flora Kluge⁵, Katja Bigge⁵, and Klaus Pfeilsticker⁵

¹Institute of Environmental Physics, University of Bremen, Bremen, Germany

²Institute of Energy and Climate Research, IEK-8: Troposphere,
Forschungszentrum Jülich GmbH, Jülich, Germany

³Institute of Meteorology and Climate Research, Karlsruhe Institute of Technology, Karlsruhe, Germany

⁴Institut für Physik der Atmosphäre, Deutsches Zentrum für Luft- und Raumfahrt (DLR),
Oberpfaffenhofen, Germany

⁵Institute of Environmental Physics, University of Heidelberg, Heidelberg, Germany

^anow at: School of Chemistry, University of Leeds, Leeds, United Kingdom

^bnow at: Flight Experiments, DLR, Oberpfaffenhofen, Germany

Correspondence: Midhun George (m.george@leeds.ac.uk) and Maria Dolores Andrés Hernández (lola@iup.physik.uni-bremen.de)

Received: 15 February 2022 – Discussion started: 18 February 2022

Revised: 3 May 2023 – Accepted: 9 May 2023 – Published: 14 July 2023

Abstract. In this study, airborne measurements of the sum of hydroperoxyl (HO₂) and organic peroxy (RO₂) radicals that react with nitrogen monoxide (NO) to produce nitrogen dioxide (NO₂), coupled with actinometry and other key trace gases measurements, have been used to test the current understanding of the fast photochemistry in the outflow of major population centres. The measurements were made during the airborne campaign of the EMeRGe (Effect of Megacities on the transport and transformation of pollutants on the Regional to Global scales) project in Europe on board the High Altitude and Long Range Research Aircraft (HALO). The measurements of RO₂^{*} on HALO were made using the in situ instrument Peroxy Radical Chemical Enhancement and Absorption Spectrometer (PeRCEAS). RO₂^{*} is a good approximation the sum of peroxy radicals reacting with NO to produce NO₂. RO₂^{*} mixing ratios up to 120 pptv were observed in air masses of different origins and composition under different local actinometric conditions during seven HALO research flights in July 2017 over Europe.

Radical production rates were estimated using knowledge of the photolysis frequencies and the RO₂^{*} precursor concentrations measured on board, as well as the relevant rate coefficients. Generally, high RO₂^{*} concentrations were measured in air masses with high production rates. In the air masses investigated, RO₂^{*} is primarily produced by the reaction of O¹D with water vapour and the photolysis of nitrous acid (HONO) and of the oxygenated volatile organic compounds (OVOCs, e.g. formaldehyde (HCHO) and glyoxal (CHOCHO)). Due to their short lifetime in most environments, the RO₂^{*} concentrations are expected to be in a photostationary steady state (PSS), i.e. a balance between production and loss rates is assumed. The RO₂^{*} production and loss rates and the suitability of PSS assumptions to estimate the RO₂^{*} mixing ratios and variability during the airborne observations are discussed. The PSS assumption for RO₂^{*} is considered robust enough to calculate RO₂^{*} mixing ratios for most conditions encountered in the air masses measured. The similarities and discrepancies between measured and PSS calculated RO₂^{*} mixing ratios are discussed. The dominant terminating processes for RO₂^{*} in the pollution plumes measured up to 2000 m are the formation of nitrous acid, nitric acid, and organic nitrates. Above

2000 m, HO₂–HO₂ and HO₂–RO₂ reactions dominate the RO₂^{*} removal. RO₂^{*} calculations by the PSS analytical expression inside the pollution plumes probed often underestimated the measurements. The underestimation is attributed to the limitations of the PSS equation used for the analysis. In particular, this expression does not account for the yields of RO₂^{*} from the oxidation and photolysis of volatile organic compounds, VOCs, and OVOCs other than those measured during the EMERGe research flights in Europe. In air masses with NO mixing ratios ≤ 50 pptv and low VOC/NO ratios, the RO₂^{*} measured is overestimated by the analytical expression. This may be caused by the formation of H₂O and O₂ from OH and HO₂, being about 4 times faster than the rate of the OH oxidation reaction of the dominant OVOCs considered.

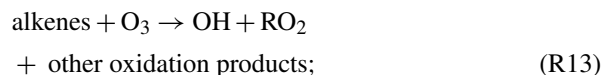
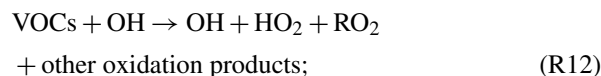
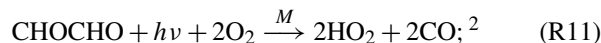
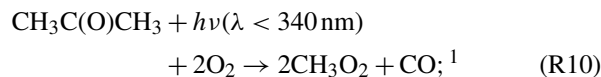
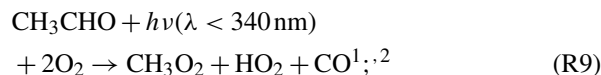
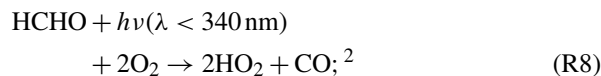
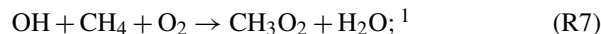
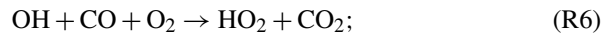
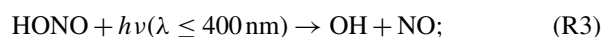
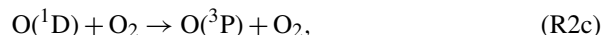
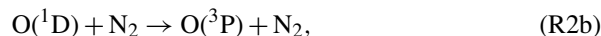
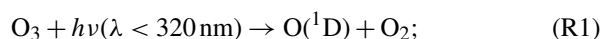
1 Introduction

Hydroperoxyl (HO₂) and organic peroxy (RO₂, where R stands for any organic group) radicals are reactive species that play a key role in the chemistry of the troposphere. In combination with the hydroxyl (OH) radical, HO₂ and RO₂ take part in rapid chemical processes that control the lifetime of many key trace constituents in the troposphere. Examples of key tropospheric processes involving HO₂ and RO₂ are as follows:

- the catalytic cycles which produce and destroy ozone (O₃);
- the generation of inorganic acids, which are precursors of aerosol and important chemical constituents in both summer and winter smog (e.g. sulfuric acid, H₂SO₄, and nitric acid, HNO₃);
- the generation of organic acids and the production of hygroscopic hydrogen peroxide (H₂O₂) and organic peroxides (ROOH), which enter aerosol and cloud droplets;
- the generation of organic peroxy nitrates (RO₂NO₂), peroxyacetyl nitrate (CH₃COO₂NO₂, PAN), and other summer smog constituents.

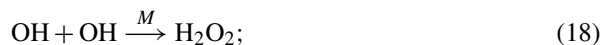
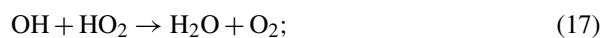
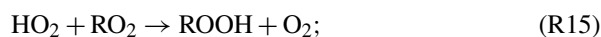
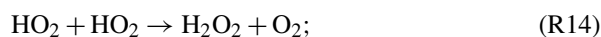
The abundance of HO₂ and RO₂ in the free troposphere has a non-linear and complex dependency on photochemistry, initiated by solar actinic radiation, and on the concentration of the precursors, such as carbon monoxide (CO), volatile organic compounds (VOCs), and peroxides. It also strongly depends on the amounts of nitrogen monoxide (NO) and nitrogen dioxide (NO₂) due to the gas-phase reactions of NO and NO₂ with the OH and organic oxy (RO) radicals formed during the radical interconversion. The main production and loss processes of HO₂ and RO₂ in the troposphere are summarised as follows:

1. Production processes of HO₂ and RO₂:

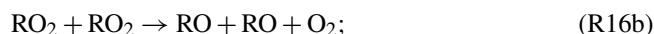


¹The CH₃ produced from the oxidation of CH₄ or the photolysis of VOCs further reacts with O₂ to form CH₃O₂. The net or overall reaction is used, because the formation of CH₃O₂ is much faster than the CH₃ formation due to the high amount of O₂ present in the atmosphere.

²H and CHO formed through the VOC photolysis further react with O₂ to form HO₂. The net or overall reaction is used, because the formation of HO₂ is much faster than the H and CHO formation due to the high amount of O₂ present in the atmosphere.

2. Loss processes of HO₂ and RO₂:

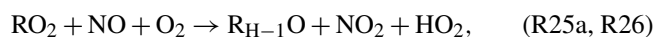
In addition, HO₂ and RO₂ participate in radical interconversion reactions such as



Reactions (R23) and (R25a) are two of the most important reactions in the troposphere as they lead to O₃ formation via Reactions (R27) and (R28). The rate of Reaction (R22) in the atmosphere compared to that of Reaction (R26) is negligible.

The sum of HO₂ and RO₂ that react with NO to produce NO₂ can be estimated by assuming that the interconversion of NO to NO₂ reaches a photostationary steady state (PSS), in which production and loss of NO₂ are to a good approximation equal.

The PSS assumption for [NO₂] in the following mechanism (Reactions R23 to R29) leads to Eq. (1):



$$[\text{HO}_2 + \text{RO}_2]_{\text{PSS}} = \frac{k_{\text{NO}+\text{O}_3}}{k_{\text{NO}+(\text{HO}_2+\text{RO}_2)}} \left(\frac{j_{\text{NO}_2} [\text{NO}_2]}{k_{\text{NO}+\text{O}_3} [\text{NO}]} - [\text{O}_3] \right) \quad (1)$$

where j_{NO_2} is the photolysis frequency of NO₂; $k_{\text{NO}+\text{O}_3}$ ($1.9 \times 10^{-14} \text{ cm}^3 \text{ molecules}^{-1} \text{ s}^{-1}$ at 298 K and 1 atm) is the rate coefficient of the reaction of NO with O₃; and $k_{\text{NO}+(\text{HO}_2+\text{RO}_2)}$ is usually estimated for the most abundant peroxy radicals HO₂ and CH₃O₂ by assuming a

1 : 1 HO₂ to CH₃O₂ ratio and averaging the $k_{\text{NO}+\text{HO}_2}$ ($8.2 \times 10^{-12} \text{ cm}^3 \text{ molecules}^{-1} \text{ s}^{-1}$ at 298 K and 1 atm) and $k_{\text{NO}+\text{CH}_3\text{O}_2}$ ($7.7 \times 10^{-12} \text{ cm}^3 \text{ molecules}^{-1} \text{ s}^{-1}$ at 298 K and 1 atm) rate coefficients for the reaction with NO. As noted by Parrish et al. (1986), the PSS assumption for NO₂ requires conditions with sufficient and stable solar irradiation, ensuring stable j_{NO_2} .

The radical calculation made on the assumption of the NO₂ steady state is very sensitive to the accuracy of the NO₂ to NO ratio and the O₃ measurements. The comparison of [HO₂ + RO₂]_{PSS} calculated using Eq. (1) with ground-based (e.g. Ridley et al., 1992; Cantrell et al., 1997; Carpenter et al., 1998; Volz-Thomas et al., 2003) as well as airborne measurements has shown in the past different degrees of agreement. The underestimations and overestimations found in air masses with different chemical compositions are not well understood. For the case of airborne measurements, the NO₂ steady-state calculation generally overestimates the measured peroxy radicals (Cantrell et al., 2003a, b). The differences observed could not be attributed to systematic changes in NO, altitude, water vapour, or temperature, although these variables are often correlated. The NO to NO₂ ratio calculated from NO measured using an in situ technique and NO₂ measured using remote sensing (more detail about the measurement techniques is given in Table 1) used in this study is considered not to have sufficient accuracy to calculate [HO₂+RO₂] from the NO₂ steady-state approach.

Ground-based (Mihelcic et al., 2003; Kanaya et al., 2007, 2012; Elshorbany et al., 2012; Lu et al., 2012, 2013; Tan et al., 2017, 2018; Whalley et al., 2018, 2021; Lew et al., 2020) and airborne (Crawford et al., 1999; Tan et al., 2001; Cantrell et al., 2003b) measurements have also been compared with model simulations of HO₂ and RO₂. The discrepancies encountered depend upon the chemical composition of the air mass and the chemical mechanisms and constraints used in the model simulations. Recently, Tan et al. (2019) and Whalley et al. (2021) reported experimental radical budget calculations using the PSS assumption for OH, HO₂, and RO₂ together with the published reaction rate coefficients of Reactions (R1) to (R26), which control OH, HO₂, and RO₂ in the lower troposphere, and the ground-based measurements of all relevant reactants and photolysis frequencies. In this study, a similar approach has been used (i.e. the sum of HO₂ and RO₂ is assumed to be in PSS) to calculate the amount of peroxy radicals in the air masses measured on board of the High Altitude and Long Range Research Aircraft (HALO) over Europe during the first campaign of the EMeRGe (Effect of Megacities on the transport and transformation of pollutants on the Regional to Global scales) project. The available onboard measurements of RO₂^{*} are defined as the total sum of OH, RO, and peroxy radicals (i.e. RO₂^{*} = OH + ∑RO + HO₂ + ∑RO₂, where RO₂ are the organic peroxy radicals producing NO₂ in their reaction with NO). As the amount of OH and RO is much smaller, RO₂^{*} to a good approximation is the sum of HO₂ and those RO₂

radicals that react with NO to produce NO₂. For the calculation, RO₂^{*} is assumed to be in PSS, and an analytical expression is developed with a manageable degree of complexity to estimate the concentration and mixing ratios of RO₂^{*}. The simultaneous onboard measurements of trace gases and photolysis frequencies are used to constrain the estimate of the RO₂^{*} concentration.

In contrast to other experimental deployments, the concentrations and/or mixing ratios of the majority of the key species involved in Reactions (R1) to (R26) were continuously measured on board HALO during the EMeRGe campaign. This enables the use of a large number of measurements to constrain the PSS calculation of RO₂^{*}. Consequently, this data set provides an excellent opportunity to gain deeper insight into the source and sink reactions of RO₂^{*} and the applicability of the PSS assumption for the different pollution regimes and related weather conditions in the free troposphere.

2 EMeRGe field campaign in Europe

The overarching objective of the EMeRGe project is to test and improve the current understanding of the photochemical and heterogeneous processing of pollution outflows from major population centres (MPCs) and their impact on the atmosphere. Two intensive observational periods (IOPs) were carried out to investigate selected European and Asian MPC outflows. The European IOP took place from 10 to 28 July 2017 (<http://www.iup.uni-bremen.de/emerge/home/home.html>, last access: 19 June 2023). An extensive set of in situ and remote sensing airborne measurements of trace gases and aerosol particles were made on board the HALO aircraft (see <http://www.halo-spp.de>, last access: 19 June 2023) along flight tracks in the lower layers of the troposphere from northwest Europe to the Mediterranean region.

During EMeRGe in Europe, HALO made a total of 53 flight hours distributed over seven flights to investigate the chemical composition of the outflows from the target MPCs: London, Paris, Benelux, Ruhr metropolitan area, Po Valley, and urban agglomerations such as Rome, Madrid, and Barcelona. The flight tracks are shown in Fig. 1. All measurement flights started from the aircraft hangar at the DLR in Oberpfaffenhofen, southwest of Munich, Germany. To achieve the scientific goals, 60 % of the flights flew at altitudes below 3000 m. Vertical profiles of trace constituents were typically made by keeping the flight altitude constant at different flight levels upwind and downwind of the target MPCs. The flights are named E-EU-FN, where E stands for EMeRGe, EU for Europe, and FN is the two-digit flight number. More details about the EMeRGe IOP in Europe and the set of instruments deployed on board the HALO aircraft are described elsewhere (Andrés Hernández et al., 2022).

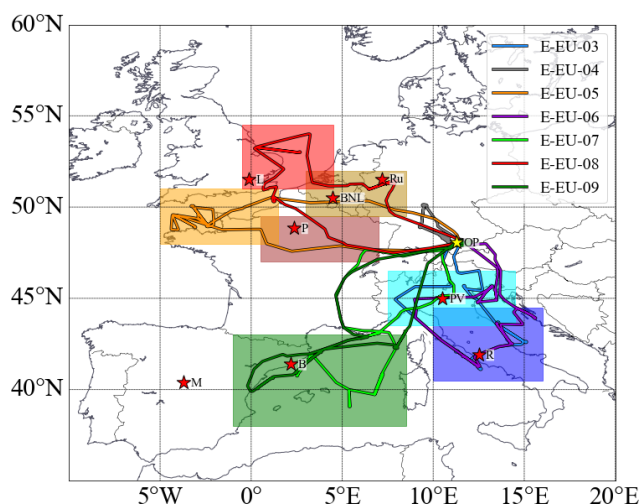


Figure 1. The research flight tracks made by HALO during the EMeRGe Europe campaign on 11, 13, 17, 20, 24, 26 and 28 July 2017 (E-EU-03 to E-EU-09, respectively, colour coded). MPC target areas are colour coded by shading, and the targeted locations/regions are marked with red stars, M: Madrid, B: Barcelona, P: Paris, L: London; BNL: Benelux; Ru: Ruhr area; PV: Po Valley, R: Rome. The location of the aircraft hangar at the DLR in Oberpfaffenhofen (OP), Germany, is indicated by a yellow star.

3 PerCEAS and other instruments on board HALO during EMeRGe

The RO₂^{*} measurements on board HALO during EMeRGe were made using the Peroxy Radical Chemical Enhancement and Absorption Spectrometer (PerCEAS). PerCEAS combines the peroxy radical chemical amplification (PerCA) and cavity ring-down spectroscopy (CRDS) techniques in a dual-channel instrument. Each channel has a separate chemical reactor and detector, which operate alternatively in both background and amplification modes to account for the rapid background variations during airborne measurements. In both modes, NO is continuously added to the air sampled at the reactor, while CO is only added in the amplification mode to initiate the chain conversion of RO₂^{*} into NO₂. In the amplification mode, the sum of the NO₂ produced from ambient RO₂^{*} through the chain reaction, the ambient NO₂, the NO₂ produced from the ambient O₃–NO reagent gas reaction, and the NO₂ produced in the inlet from any other sources (e.g. thermal decomposition of PAN) is measured. In the background mode, the sum of the ambient NO₂, the NO₂ produced from the ambient O₃–NO reagent gas reaction, and NO₂ produced in the inlet from any other sources is measured. The RO₂^{*} is retrieved by dividing the difference in NO₂ concentration (ΔNO_2) between amplification and background mode by the conversion efficiency of RO₂^{*} to NO₂, which is referred to as eCL (effective chain length). The PerCEAS instrument and its specifications have been

described in detail elsewhere (Horstjann et al., 2014; George et al., 2020; George, 2022).

The two chemical reactors for sampling the ambient air are part of the DUAL channel Airborne peroxy radical Chemical Amplifier (DUALER) inlet installed inside a pylon located on the outside of the HALO fuselage. During the EMeRGe campaign in Europe, a reagent gas mixing ratio of 30 ppmv NO ($[\text{NO}] = 1.46 \times 10^{14}$ molecules cm^{-3} at 296 K, 200 mbar) and of 9 % CO ($[\text{CO}] = 4.4 \times 10^{17}$ molecules cm^{-3} at 296 K, 200 mbar) was added to the sample flow for the chemical conversion of RO_2^* to NO_2 . The DUALER inlet was operated at an internal pressure of 200 mbar to achieve stable chemical conversion. The HO_2 and RO_2 detection sensitivity depends on the rates of loss of HO_2 and RO_2 by Reactions (R19) and (R22). The latter depends on the concentration of the reagent gas NO added and the reaction rate coefficients, where k_{22} is larger than k_{19} . The average eCL for a 1 : 1 HO_2 to CH_3O_2 mixture under the DUALER conditions during the campaign in Europe was determined to be 50 ± 8 from laboratory calibrations, where the error is the $\pm 1\sigma$ standard deviation estimated from the reproducibility of the experimental determinations. Likewise, the ratio $\alpha = \text{eCL}_{\text{CH}_3\text{O}_2} / \text{eCL}_{\text{HO}_2}$ was determined to be 65 % for the measurement conditions (George et al., 2020). The values obtained from calibrations before and after the campaign agreed within their experimental errors.

Although the DUALER pressure is kept constant below the ambient pressure, variations in dynamical pressure > 10 mbar during the flight change the residence time and induce turbulence inside the inlet (Kartal et al., 2010; George et al., 2020). These may lead to different physical losses of radicals before amplification and affect the eCL. In the measurements presented in this study, variations in dynamical pressure of this magnitude were only encountered during flight level changes of the aircraft. When used during the analysis, these data sets are either excluded or flagged (P_flag). The effect of the ambient air humidity on eCL (Mihele and Hastie, 1998; Mihele et al., 1999; Reichert et al., 2003) has been accounted for by a calibration procedure reported in George et al. (2020). The $[\text{H}_2\text{O}]$ in the DUALER inlet was lower than 1×10^{17} molecules cm^{-3} for 60 % of measurements during EMeRGe in Europe, for which the $\text{eCL}_{\text{wet}} = 76$ % of eCL_{dry} . At the highest humidity observed during the campaign, i.e. $[\text{H}_2\text{O}]_{\text{inlet}} = 2 \times 10^{17}$ molecules cm^{-3} , the eCL_{wet} is 55 % of eCL_{dry} (see Fig. S1 in the Supplement).

In addition to the measurement of RO_2^* from PeRCEAS, other in situ and remote sensing measurements and basic aircraft data from HALO are used in this study. Details of the corresponding instruments are summarised in Table 1. The remote sensing instruments used on HALO during EMeRGe were the mini-differential optical absorption spectrometer (miniDOAS) and the Heidelberg airborne imaging DOAS instrument (HAIDI). The miniDOAS observes the atmosphere using six telescopes: two being optimised for the ultraviolet, two for the visible, and two for the near-infrared (nIR). Three

telescopes observe in nadir-viewing mode and three in limb-viewing mode. The three limb scanning telescopes point to the starboard side perpendicular to the aircraft fuselage axis. They are rotated to compensate for roll relative to the horizon. A variant of the DOAS retrieval technique uses least square fitting of the measured and radiative transfer modelled absorption along the line of sight to retrieve the differential slant column density (dSCD) of the target gas and a scaling reference gas. The latter is the dimer of molecular oxygen (O_4). As the vertical profile of the concentrations of O_2 and thus O_4 are known, the mixing ratios of the target gas at the flight altitude are obtained from the target gas and O_4 dSCDs (for more details, see Stutz et al., 2017; Hüneke et al., 2017; Kluge et al., 2020; and Rotermund et al., 2021). The HAIDI nadir observations are used to retrieve dSCDs below the aircraft. The dSCDs from HAIDI are then converted to mixing ratios using knowledge of the aircraft altitude and the corresponding geometric air mass factor (AMF), calculated by a radiative transfer model under a well-mixed NO_2 layer assumption. As a result of this assumption, the calculated mixing ratios for HAIDI target gases are lower limits and similar to the actual values while flying within and close to a well-mixed boundary layer. In spite of the differences in sampling volume and temporal and spatial resolution between the in situ and remote sensing measurement techniques, the concentrations of the gas HCHO measured by both techniques were in good agreement, and the concentrations of the NO_2 (remote sensing) and NO_y (in situ) were consistent (for more details, see Schumann, 2020).

4 Results and discussion

4.1 Airborne RO_2^* measurements during EMeRGe in Europe

RO_2^* mixing ratios up to 120 pptv were measured during the campaign, as shown in Fig. 2. Typically, the highest RO_2^* mixing ratios were observed below 3000 m over southern Europe.

The origin and thus the composition of the air sampled during the seven flights over Europe were different and heterogeneous. Typically, the air masses measured were influenced by emissions from MPCs and their surroundings and sometimes by biomass burning transported over short or long distances. The concentration and mixing ratio of RO_2^* rather depends on the insolation and the chemical composition of the air probed, particularly on the abundance of RO_2^* precursors, than on the origin of the air masses. Since RO_2^* species are controlled by fast chemical and photochemical processes, the air mass origin and trajectory are not used in the calculation of RO_2^* concentrations and mixing ratios but are of interest as the source of RO_2^* precursors. Thus, the RO_2^* variability and its production rates provide valuable insight into the photochemical activity of the air masses probed.

Table 1. List of the airborne measurements and instrumentation used in this study. PeRCA: peroxy radical chemical amplification; CRDS: cavity ring-down spectroscopy; PTR-MS: proton-transfer-reaction mass spectrometer; AT-BS: adsorption tube and bag air sampler; TD-GC-MS: thermal desorption gas chromatography and mass spectrometry; DOAS: differential optical absorption spectrometry; Univ.: University; KIT: Karlsruher Institut für Technologie; DLR: Deutsches Zentrum für Luft- und Raumfahrt; IPA: Institut für Physik der Atmosphäre; FZ: Forschungszentrum; FX: Flugexperimente; HKMS: HALO Karlsruher Mass Spectrometer; VUV: visible-UV; SR: spectroradiometer; BAHAMAS: Basic Halo Measurement and Sensor System; FAIRO: Fast Accurate aIRborne Ozone instrument; CATS: cavity ring-down spectrometer and Tedlar bag sampler.

Trace gas in situ measurements				
Species/parameters	Acronym	Institution	Technique/instrument	Reference
$\text{RO}_2^* = \text{HO}_2 + \sum \text{RO}_2$	PeRCEAS	Univ. Bremen	PeRCA + CRDS	George et al. (2020)
OVOC	HKMS	KIT Karlsruhe	PTR-MS	Brito and Zahn (2011)
O_3	FAIRO	KIT Karlsruhe	UV photometry/chemiluminescence	Zahn et al. (2012)
O_3, CO	AMTEX	DLR-IPA	UV photometry/VUV fluorimetry	Gerbig et al. (1996)
NO, NO_y	AENEAS	DLR-IPA	Chemiluminescence/gold converter	Ziereis et al. (2004)
CO_2, CH_4	CATS	DLR-IPA	CRDS	Chen et al. (2010)
Trace gas remote sensing measurements				
Species/parameters	Acronym	Institution	Technique/instrument	Reference
$\text{NO}_2, \text{HONO}, \text{CH}_2\text{O}, \text{C}_2\text{H}_2\text{O}_2, \text{C}_3\text{H}_4\text{O}_2$	miniDOAS	Univ. Heidelberg	DOAS/UV-nIR; 2D optical spectrometer	Hüneke et al. (2017)
NO_2	HAIDI	Univ. Heidelberg	DOAS/3 × 2D imaging spectrometers	General et al. (2014)
Other parameters				
Species/parameters	Acronym	Institution	Technique/instrument	Reference
Spectral actinic flux density (up/down), photolysis frequencies	HALO-SR	FZ Jülich	CCD spectroradiometry	Bohn and Lohse (2017)
Basic aircraft data	BAHAMAS	DLR-FX	various	Mallaun et al. (2015)

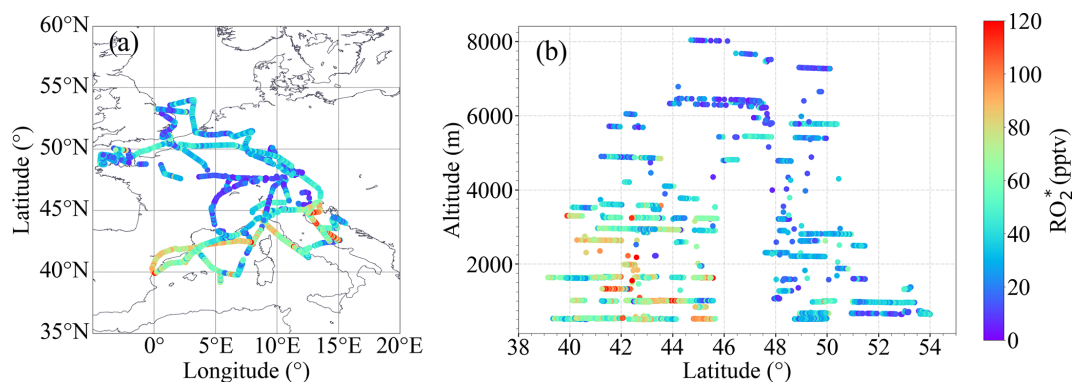


Figure 2. RO_2^* measured during EMerGe-Europe: (a) as a function of longitude and latitude and (b) as a function of latitude and altitude.

Changes in RO_2^* as a function of latitude and altitude, as shown in Fig. 2, confirm the heterogeneity of the photochemical activity in the air masses probed. Figure 3 shows the RO_2^* vertical profiles averaged for the EMerGe flights over Europe in 500 m altitude bins. The error bars are standard errors

(i.e. $\pm 1\sigma$ standard deviation of each bin). The vertical profiles may be biased as the higher altitudes have fewer measurements than those below 3000 m, as mentioned in Sect. 2. The vertical profiles are a composite from averaging flights with legs carried out at different longitudes and latitudes and

are only shown to summarise the variability in the composition of the air masses measured during the campaign.

Most of the EMeRGe measurements below 2000 m were carried out in the outflow of MPCs, which are expected to contain significant amounts of RO₂^{*} precursors. HALO flew at the lowest altitudes during flight legs over the English Channel, the Mediterranean, and the North Sea. The H₂O concentration in the air masses decreased steadily with altitude as expected. The higher relative variability in H₂O observed at 3000 m and the increase at 5000 m are associated with measurements under stormy conditions, often over the Alps.

4.2 RO₂^{*} production rates

The rate of production of RO₂^{*} from Reactions (R1) to (R13) is given by

$$P_{\text{RO}_2^*} = 2j_{\text{O}^1\text{D}}[\text{O}_3] \cdot \frac{k_{\text{O}_\text{D}^1+\text{H}_2\text{O}}[\text{H}_2\text{O}]}{k_{\text{O}_\text{D}^1+\text{H}_2\text{O}}[\text{H}_2\text{O}] + k_{\text{O}_\text{D}^1+\text{O}_2}[\text{O}_2] + k_{\text{O}_\text{D}^1+\text{N}_2}[\text{N}_2]} + j_{\text{HONO}}[\text{HONO}] + 2j_{\text{H}_2\text{O}_2}[\text{H}_2\text{O}_2] + 2\sum_i j_i[\text{OVOC}_i] + \sum k_{\text{O}_3+\text{alkenes}_k}[\text{O}_3][\text{alkenes}_k]\gamma_k, \quad (2)$$

where OVOC stands for oxygenated volatile organic compounds, and γ is the effective RO₂^{*} yield from ozonolysis of alkenes.

In this study, Eq. (2) has been applied to the measurements taken within the EMeRGe campaign in Europe. There were no H₂O₂ measurements available for EMeRGe. However, the results reported by Tan et al. (2001) indicate that the rate of OH production from the H₂O₂ photolysis is not significant except when NO_x is low. To be more precise, for conditions having NO < 50 ppt, the partitioning of HO_x is strongly shifted to HO₂. HO₂ then predominantly reacts with itself or RO₂ to form peroxides, which can in turn photolyse. For conditions with NO > 50 pptv, the rates of reactions of HO_x with NO_x are faster than those of HO₂ with HO₂ and RO₂. As the NO mixing ratio was higher than 50 pptv in 75 % of the air masses probed in Europe, the photolysis of H₂O₂ was as a first approximation assumed not to be a significant source of OH for the EMeRGe data set considered in this study.

Formaldehyde (HCHO), acetaldehyde (CH₃CHO), acetone (CH₃C(O)CH₃), and glyoxal (CHOCHO) were the OVOCs measured in EMeRGe directly forming radicals through photolysis. They are produced in the photolysis and oxidation of VOCs and are likely the most abundant and reactive OVOCs present. In this study they were assumed to be the dominant VOCs in the air masses probed.

There were no measurements of alkenes provided in EMeRGe. Consequently, the ozonolysis term in Eq. (2) was not included in the analysis.

The above assumptions lead to Eq. (3), which calculates the RO₂^{*} production rate ($P_{\text{RO}_2^*}$) for the EMeRGe measurements as follows:

$$P_{\text{RO}_2^*} = 2j_{\text{O}^1\text{D}}[\text{O}_3] \cdot \frac{k_{\text{O}_\text{D}^1+\text{H}_2\text{O}}[\text{H}_2\text{O}]}{k_{\text{O}_\text{D}^1+\text{H}_2\text{O}}[\text{H}_2\text{O}] + k_{\text{O}_\text{D}^1+\text{O}_2}[\text{O}_2] + k_{\text{O}_\text{D}^1+\text{N}_2}[\text{N}_2]} + j_{\text{HONO}}[\text{HONO}] + 2j_{\text{HCHO}}[\text{HCHO}] + 2j_{\text{CH}_3\text{CHO}}[\text{CH}_3\text{CHO}] + 2j_{\text{CH}_3\text{C}(\text{O})\text{CH}_3}[\text{CH}_3\text{C}(\text{O})\text{CH}_3] + 2j_{\text{CHOCHO}}[\text{CHOCHO}]. \quad (3)$$

The production rate of RO₂^{*} molecules can be expressed in units of mixing ratio of RO₂^{*} by dividing with the air concentration at each altitude, calculated from the pressure and temperature measurements (for the vertical profile and the latitudinal distribution of $P_{\text{RO}_2^*}$, see Figs. S2 and S3 in the Supplement). Figure 4 shows the composite averaged vertical profile of all measured RO₂^{*} mixing ratios colour-coded with the calculated $P_{\text{RO}_2^*}$. For the sake of representativeness and comparability, the number of measurements in each altitude bin is shown in Fig. 4b. The higher RO₂^{*} mixing ratios observed below 4000 m are typically associated with $P_{\text{RO}_2^*} \geq 0.4$ pptv s⁻¹. Above 4000 m, both $P_{\text{RO}_2^*}$ and RO₂^{*} start to decrease with altitude, as expected. This is related to the decrease in H₂O and other radical precursor concentrations with altitude, as detailed in Figs. 5 and 6. In previous airborne campaigns at various parts of the world, RO₂^{*} vertical distributions showed a local maximum between 1500 and 4000 m, as reported by Tan et al. (2001), Cantrell et al. (2003a, b), and Andrés-Hernández et al. (2009). In the present work, this local maximum is more evident for measurements with $P_{\text{RO}_2^*} \geq 0.5$ pptv s⁻¹.

Figure 5 shows the fractional contribution of the production rate from each radical precursor reaction included in Eq. (3) as a function of altitude. The data are classified into three groups according to the rate of change of production of the RO₂^{*} mixing ratio: $P_{\text{RO}_2^*} < 0.07$ pptv s⁻¹ (Fig. 5a), $0.07 < P_{\text{RO}_2^*} < 0.8$ pptv s⁻¹ (Fig. 5b), and $P_{\text{RO}_2^*} > 0.8$ pptv s⁻¹ (Fig. 5c) to show the lowest, most common, and highest ranges, respectively, encountered during the campaign. For 89 % of the measurements, $0.07 < P_{\text{RO}_2^*} < 0.8$ pptv s⁻¹ applies, while the rest of the data are equally distributed in the other two $P_{\text{RO}_2^*}$ ranges. The data in each group are always binned over 500 m when available.

Typically, the high amount of H₂O in the air masses probed leads to the reaction of O¹D with H₂O (Reactions R1–R2a), being the highest RO₂^{*} radical production rate (≥ 50 %) below 4000 m. As the amount of H₂O reduces with altitude, the relative contribution from O₃ photolysis decreases. Above 4000 m, HCHO, HONO, and CHOCHO photolysis contributions range between 20 % to 40 %, 2.5 % to 30 %, and 5 % to 25 %, respectively. The HCHO contribution

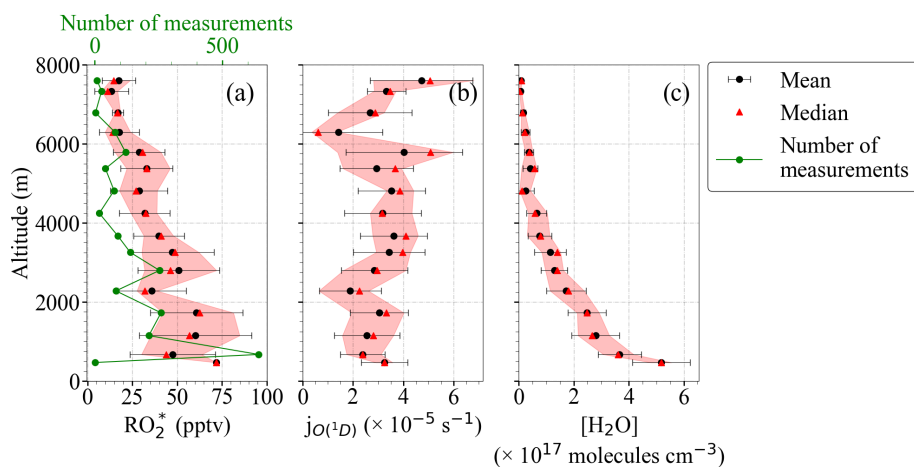


Figure 3. Composite average vertical profiles of (a) RO_2^* , (b) $j_{\text{O}(^1\text{D})}$, and (c) $[\text{H}_2\text{O}]$ observations. The measurements are binned over 500 m altitude. The error bars are the $\pm 1\sigma$ standard deviation of each bin. Median values (red triangles), the interquartile 25%–75% range (shaded red area), and the number of individual measurements for each bin (in green) are additionally plotted.

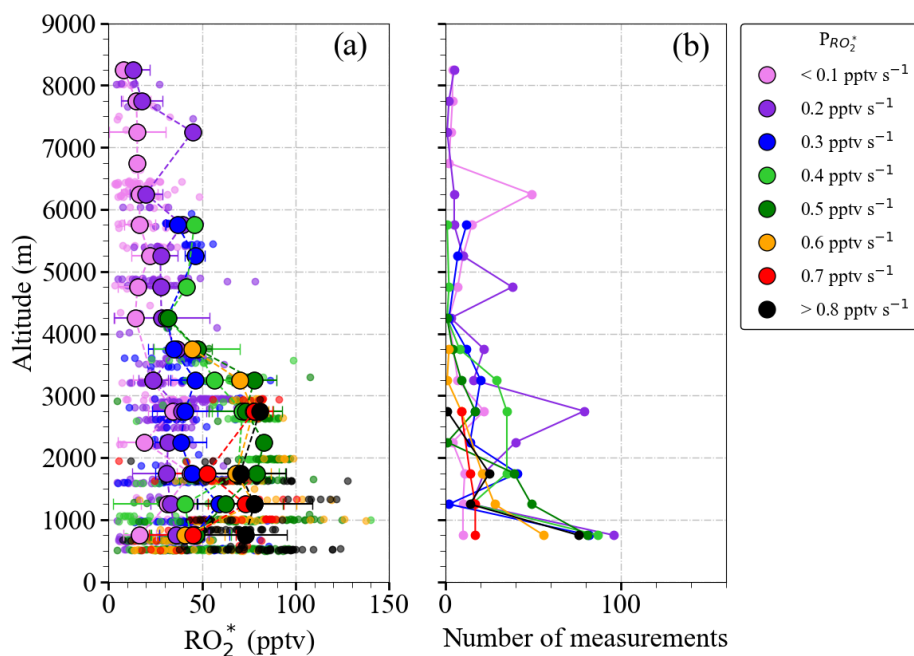


Figure 4. (a) Composite averaged vertical distribution of measured RO_2^* colour-coded according to the value of $P_{\text{RO}_2^*}$; (b) the number of measurements in each altitude bin. Small circles are 1 min individual measurements binned with $P_{\text{RO}_2^*}$ values in 0.1 pptv s^{-1} intervals. Larger circles result from a further binning over 500 m altitude steps. All the production rates below 0.1 pptv s^{-1} and above 0.8 pptv s^{-1} are binned to 0.1 and 0.8 pptv s^{-1} , respectively. The error bars are the standard deviation for each altitude bin.

increases up to 80 % during measurements above 6000 m. The contributions of CH_3CHO and $\text{CH}_3\text{C}(\text{O})\text{CH}_3$ photolysis are, in contrast, practically negligible ($< 5\%$).

The vertical changes of the precursor mixing ratios and photolysis frequencies used to calculate $P_{\text{RO}_2^*}$ in Fig. 5 are shown in Fig. 6a to f. $P_{\text{RO}_2^*} < 0.07 \text{ pptv s}^{-1}$ is associated with measurements under cloudy conditions, towards sunset where the photolysis frequencies are low, or at alti-

tudes above 5000 m in air masses with a low amount of RO_2^* precursors. Values of $P_{\text{RO}_2^*} > 0.8 \text{ pptv s}^{-1}$ are found for air masses, measured below 2000 m in the outflow of MPCs over the sea, for conditions having sufficient insolation ($j_{\text{O}(^1\text{D})} > 3 \times 10^{-5} \text{ s}^{-1}$) and a high content of RO_2^* precursors ($\text{HCHO} > 1000 \text{ pptv}$ and $\text{HONO} > 100 \text{ pptv}$). The increase in the photolysis frequencies as a function of altitude is concurrent with decreases in precursor concentrations. As

a result, the $P_{\text{RO}_2^*}$ rates do not significantly vary with altitude in the air masses investigated.

In previous airborne campaigns, Tan et al. (2001) and Cantrell et al. (2003b) reported a reduction of the fractional contribution of the reaction of $\text{O}(^1\text{D})$ with H_2O as the $P_{\text{RO}_2^*}$ value decreases. At very low $P_{\text{RO}_2^*}$ values (< 0.03 pptv s^{-1}), the sum of all other production terms exceeded the fraction from the $\text{O}(^1\text{D}) + \text{H}_2\text{O}$ term. For these conditions, H_2O_2 and VOCs photolysis dominated $P_{\text{RO}_2^*}$. For the EMeRGe data set in Europe, only 6 % of $P_{\text{RO}_2^*}$ is below 0.06 pptv s^{-1} .

4.3 PSS estimation of the RO_2^* mixing ratios

Under most ambient conditions in the troposphere, the RO_2^* species are short-lived, and the chemical lifetime of RO_2^* is much shorter than the chemical transport time into and out of an air mass being probed. Consequently, pseudo-steady-state conditions prevail, and the radical production and destruction rates are balanced:

$$P_{\text{RO}_2^*} = D_{\text{RO}_2^*}. \quad (4)$$

The Reactions (R5) to (R7), (R12), (R16b), and (R23) to (R26) are interconversion reactions between OH, RO, HO_2 , and RO_2 and do consequently occur without radical losses. Solving Eq. (4) leads to Eq. (5) if $\text{RO}_2^* - \text{RO}_2^*$ reactions are assumed to be the dominant radical terminating processes.

$$2j_{\text{O}(^1\text{D})}[\text{O}_3] + \frac{k_{\text{O}_b^1 + \text{H}_2\text{O}}[\text{H}_2\text{O}]}{k_{\text{O}_b^1 + \text{H}_2\text{O}}[\text{H}_2\text{O}] + k_{\text{O}_b^1 + \text{O}_2}[\text{O}_2] + k_{\text{O}_b^1 + \text{N}_2}[\text{N}_2]} + j_{\text{HONO}}[\text{HONO}] + 2j_{\text{HCHO}}[\text{HCHO}] + 2j_{\text{CH}_3\text{CHO}}[\text{CH}_3\text{CHO}] + 2j_{\text{CH}_3\text{C}(\text{O})\text{CH}_3}[\text{CH}_3\text{C}(\text{O})\text{CH}_3] + 2j_{\text{CHOCHO}}[\text{CHOCHO}] = k_{\text{RO}_2^* + \text{RO}_2^*}[\text{RO}_2^*]^2, \quad (5)$$

where j_{HCHO} , $j_{\text{CH}_3\text{CHO}}$, $j_{\text{CH}_3\text{C}(\text{O})\text{CH}_3}$, and j_{CHOCHO} are respectively j_8 , j_9 , j_{10} , and j_{11} , as in Table S1 in the Supplement, and $k_{\text{RO}_2^* + \text{RO}_2^*}$ represents an effective RO_2^* self-reaction rate coefficient, comprising $\text{HO}_2 - \text{HO}_2$, $\text{HO}_2 - \text{RO}_2$, and $\text{RO}_2 - \text{RO}_2$ reaction rates.

Consequently, the RO_2^* concentrations are expected to correlate with the square root of the $P_{\text{RO}_2^*}$.

Figure 7 shows the relationship between the measured $[\text{RO}_2^*]$ and the calculated $\sqrt{2P_{\text{RO}_2^*}}$. Generally, both $[\text{RO}_2^*]$ and $\sqrt{2P_{\text{RO}_2^*}}$ increase with the photolysis frequency of O_3 ($j_{\text{O}(^1\text{D})}$). Measurements with $[\text{RO}_2^*] < 0.5 \times 10^{12}$ molecules cm^{-3} , $\sqrt{2P_{\text{RO}_2^*}} < 1000$, and $j_{\text{O}(^1\text{D})} > 5 \times 10^{-5}$ were made above 6000 m, where the amount of RO_2^* precursors is low. The relatively weak correlation observed between $[\text{RO}_2^*]$ and $\sqrt{2P_{\text{RO}_2^*}}$ indicates the necessity of other radical terminating processes and/or missing radical formation terms in the $P_{\text{RO}_2^*}$ calculation. Apart from this, the spread

in the diagram confirms that the effective RO_2^* self-reaction rate $k_{\text{RO}_2^* + \text{RO}_2^*}[\text{RO}_2^*]^2$ varies widely in the air masses probed, likely due to the effect of changes in HO_2 and $\sum \text{RO}_2$ concentrations in the individual loss reaction rate coefficients. Photochemical processing is expected to be enhanced over southern Europe due to the prevailing conditions of high insolation and temperatures during the EMeRGe flights, which might lead to the rapid production of RO_2^* from the photochemical oxidations of CO and VOCs. This is also reflected in the higher $P_{\text{RO}_2^*}$ and $[\text{RO}_2^*]$ observed in southern Europe as compared to those in northern Europe (Fig. 7b).

The correlation between $[\text{RO}_2^*]$ and $\sqrt{2P_{\text{RO}_2^*}}$ improves when the measurements south and north of 47°N are separately analysed (Fig. 8). For a given $[\text{RO}_2^*]$, the $P_{\text{RO}_2^*}$ calculated is higher for the measurements north of 47°N than south of 47°N . The lowest $[\text{RO}_2^*]$ to $\sqrt{2P_{\text{RO}_2^*}}$ ratios are associated with higher NO_x ($\text{NO} + \text{NO}_2$), especially north of 47°N , indicating the urban character and higher amounts of the RO_2^* precursors of the air probed (Fig. 8d). Please note that these results are only valid for the data set acquired over Europe during EMeRGe flights and do not yield a relationship between $[\text{RO}_2^*]$ and $\sqrt{2P_{\text{RO}_2^*}}$, which is generally applicable under all conditions for these two latitude windows.

The relationship between RO_2^* and $P_{\text{RO}_2^*}$ is further investigated to identify the dominant RO_2^* loss process in the air masses considered in this study. As stated in Sect. 3, HO_2 and RO_2 are not speciated but retrieved as RO_2^* by the PerRCEAS instrument. Because not all peroxy radicals are detected equally by the instrument, the comparison of measured and calculated RO_2^* values is complicated. To investigate this, the changes in the HO_2 to the total RO_2^* ratios have been taken into consideration by δ (i.e. $[\text{HO}_2] = \delta[\text{RO}_2^*]$ and $[\text{CH}_3\text{O}_2] = (1 - \delta)[\text{RO}_2^*]$) in the analysis. As a first approach, RO_2 is assumed to consist only of CH_3O_2 to reduce the complexity of the calculations by considering only CH_3O_2 reaction rate constants. The reaction channel (R25b) is not considered in the calculation since the yield of this channel is $< 5\%$ (Burkholder et al., 2019) for $\text{CH}_3\text{O}_2 + \text{NO}$ reaction. Moreover, as mentioned in Sect. 3, the ratio $\alpha = e\text{CL}_{\text{CH}_3\text{O}_2}/e\text{CL}_{\text{HO}_2}$ was determined to be 65 % for the measurement conditions (George et al., 2020).

Equation (5) is additionally extended to include RO_2^* effective yields from VOC oxidation and radical losses through HONO and HNO_3 formation:

$$(2j_1[\text{O}_3]\beta + j_3[\text{HONO}](1 - \rho) + 2j_8[\text{HCHO}] + 2j_9[\text{CH}_3\text{CHO}] + 2(j_{10a} + j_{10b})[\text{CH}_3\text{C}(\text{O})\text{CH}_3] + 2j_{11}[\text{CHOCHO}] = \delta[\text{RO}_2^*](k_{23}[\text{NO}] + k_{24}[\text{O}_3])\rho + 2k_{15}\delta(1 - \delta)[\text{RO}_2^*]^2 + 2k_{16a}((1 - \delta)[\text{RO}_2^*])^2 + 2k_{14}(\delta[\text{RO}_2^*])^2, \quad (6)$$

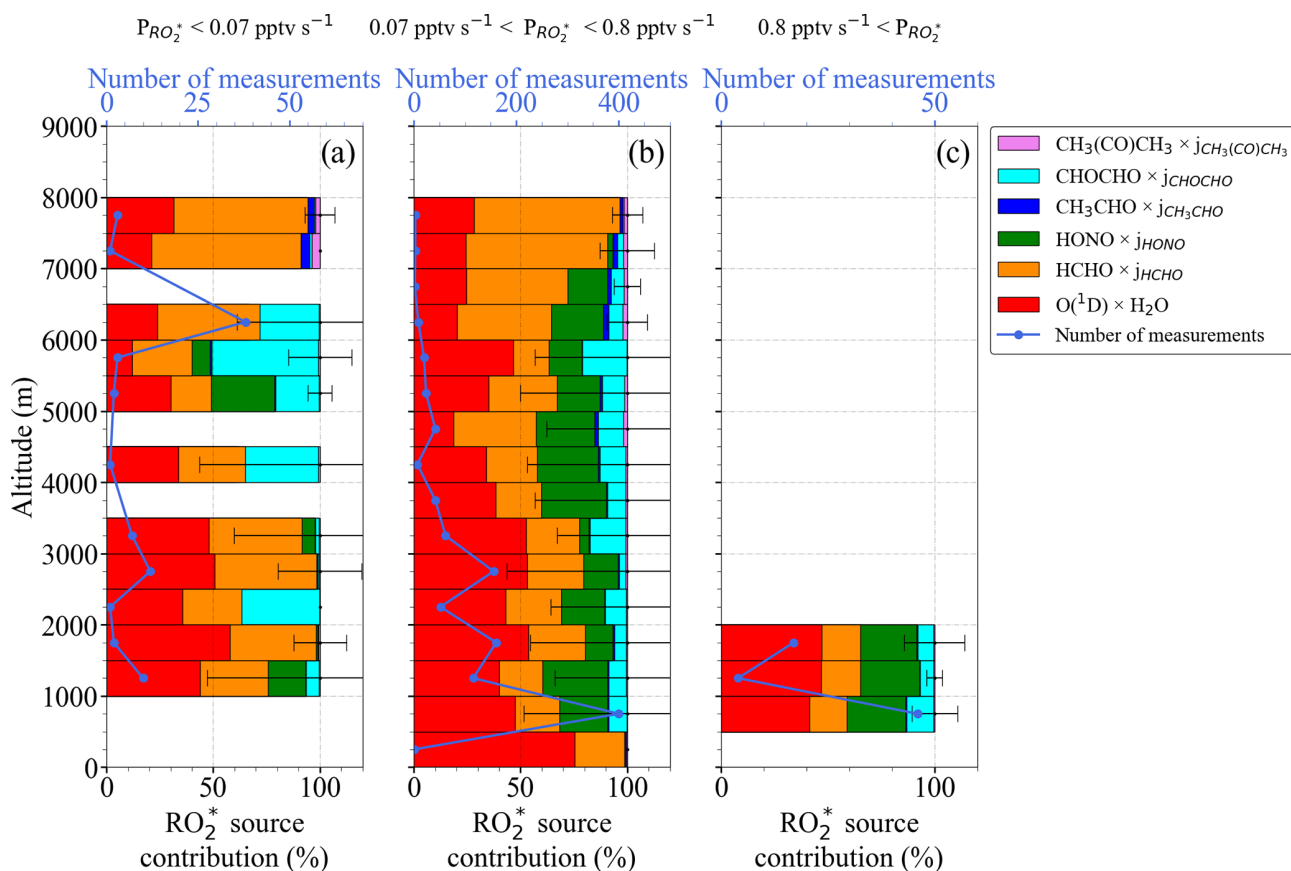


Figure 5. Total $P_{RO_2^*}$ and fractional precursor contributions estimated using Eq. (3) as a function of altitude for (a) $P_{RO_2^*} < 0.07 \text{ pptv s}^{-1}$, (b) $0.07 \text{ pptv s}^{-1} < P_{RO_2^*} < 0.8 \text{ pptv s}^{-1}$, and (c) $P_{RO_2^*} > 0.8 \text{ pptv s}^{-1}$. Note the different scales in the number of measurements.

where β is the effective yield of OH in the reaction of $O(^1D)$ with H_2O given by

$$\beta = \left(\frac{k_{2a} [H_2O]}{k_{2a} [H_2O] + k_{2b} [O_2] + k_{2c} [N_2]} \right). \quad (7)$$

On the left-hand side of Eq. (6), $1 - \rho$ accounts for the effective yield of $HO_2 + RO_2$ production through the radical initiation Reactions (R2a) and (R3) and Reactions (R5) to (R7) and (R12). As the calculation is constrained with on-board measurements, only the reactions of measured VOCs were considered in Reaction (R12). Similarly, on the right-hand side of Eq. (6), ρ accounts for the radical termination through the $OH + NO$, $OH + NO_2$, and $OH + HONO$ reactions (Reactions R19 to R21) relative to the radical undergoing OH to peroxy radical conversion.

Consequently, ρ is given by

$$\rho = \frac{(k_{19} [NO] + k_{20} [NO_2] + k_{21} [HONO])}{(k_5 [O_3] + k_6 [CO] + k_7 [CH_4] + k_{12a} [HCHO] + k_{12b} [CH_3CHO] + k_{12c} [CH_3C(O)CH_3] + k_{12d} [CH_3OH] + k_{12e} [CHOCHO] + k_{19} [NO] + k_{20} [NO_2] + k_{21} [HONO])}. \quad (8)$$

Measurements of CH_4 , $HCHO$, CH_3CHO , $CHOCHO$, CH_3OH , and $CH_3C(O)CH_3$ on board HALO are available

and implemented in Eq. (6). These comprise the most abundant and reactive OVOCs and are considered to be a representative surrogate for the VOCs that act as RO_2^* precursors through oxidation and photolysis. During the EMerGe campaign in Europe, $k_{12a} \times [HCHO]$ and $k_{12b} \times [CH_3CHO]$ have the highest contribution to $1 - \rho$ from all the OVOC measured. Their impact on the RO_2^* budget is found to be similar, because their respective concentrations compensate for the difference in the rate coefficients of their reactions with OH ($k_{12a} = 8.5 \times 10^{-12} \text{ cm}^3 \text{ molecule}^{-1} \text{ s}^{-1}$ and $k_{12b} = 1.5 \times 10^{-11} \text{ cm}^3 \text{ molecule}^{-1} \text{ s}^{-1}$ at 298 K and 1 atm). Despite its high mixing ratios measured, $CH_3C(O)CH_3$ is less important in the $1 - \rho$ term. This is because the rate coefficient $k(T)_{12c}$ is significantly slower than k_{12a} and k_{12b} (see Table S1 in the Supplement). Similarly, the contribution of $CHOCHO$ and CH_3OH is an order of magnitude lower than that of $HCHO$ and CH_3CHO .

Concerning the term $\delta [RO_2^*] (k_{23} [NO] + k_{24} [O_3]) \rho$ on the right-hand side of Eq. (6), the HO_2 reaction with O_3 has a negligible effect as k_{24} is almost 4 orders of magnitude smaller than k_{23} , and the NO concentrations remained about

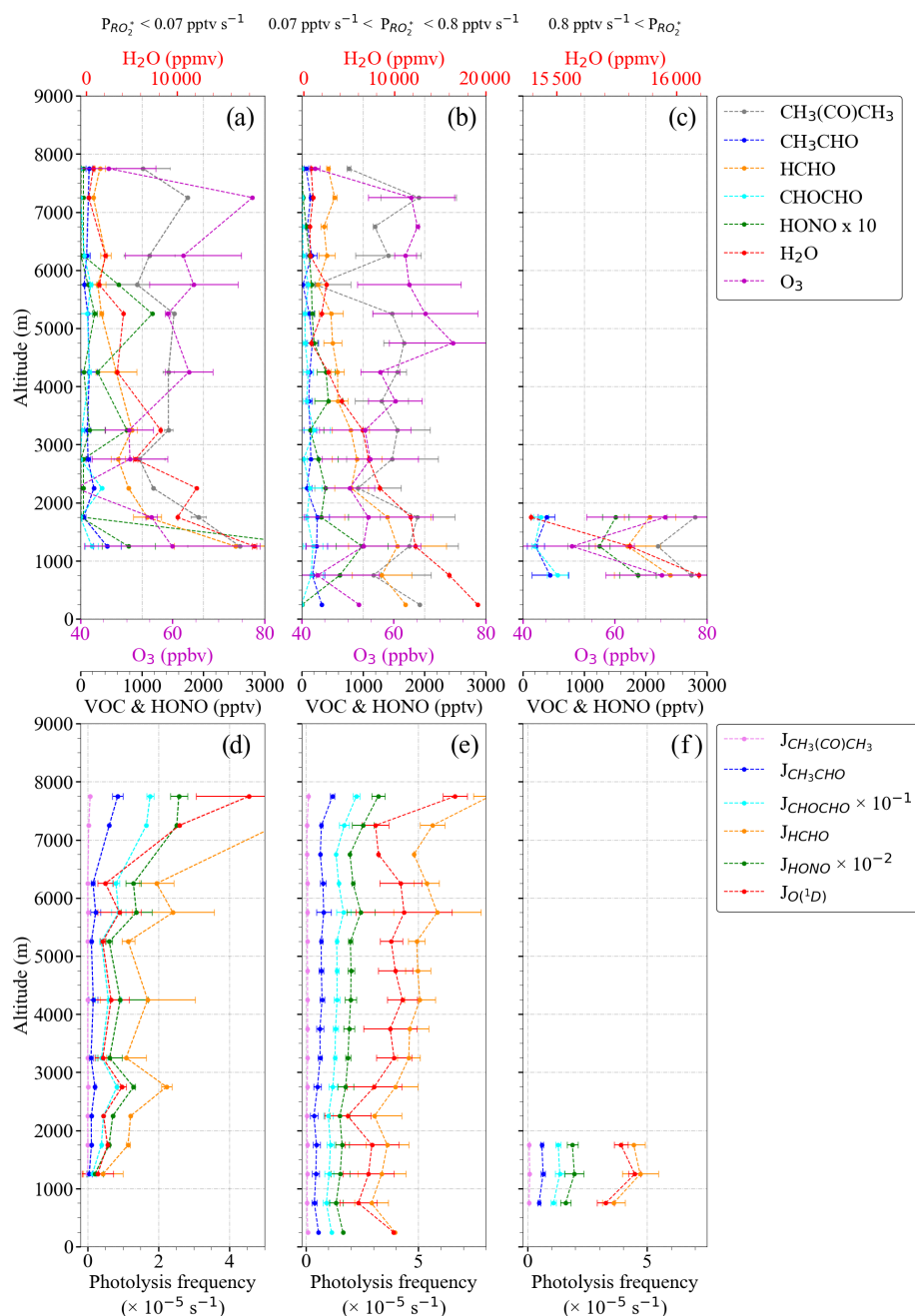


Figure 6. Vertical distribution and variation of (a) to (c) precursor mixing ratios; (d) to (f) photolysis frequencies for the $P_{RO_2^*}$ bins as in Fig. 5. Note the different scales in the H_2O concentration.

3 orders of magnitude smaller than the O_3 measured during the campaign.

The impact of the methylglyoxal ($CH_3C(O)C(O)H$) photolysis was also investigated by using the $CH_3C(O)C(O)H^*$ measurements provided by the miniDOAS instrument. The $CH_3C(O)C(O)H^*$ measured is the sum of $CH_3C(O)C(O)H$ and a fraction of other substituted dicarbonyls (mainly 2,3-butanedione, $C_3H_6O_2$), with similar visible absorption spectra. For the calculation, $CH_3C(O)C(O)H$ was assumed to

be half of $CH_3C(O)C(O)H^*$ as recommended by Zarzana et al. (2017) and Kluge et al. (2020). The RO_2^* calculated by including $CH_3C(O)C(O)H$ photolysis systematically overestimated the measurements. As the adequacy of the recommended factor of 0.5 varies with the actual air mass composition, $CH_3C(O)C(O)H$ was not included in the calculations.

Figure 9 shows the fractional contribution of the destruction rate ($D_{RO_2^*}$) calculated for a 1 : 1 mixture of HO_2 and CH_3O_2 using the reactions included in Eq. (6) as a func-

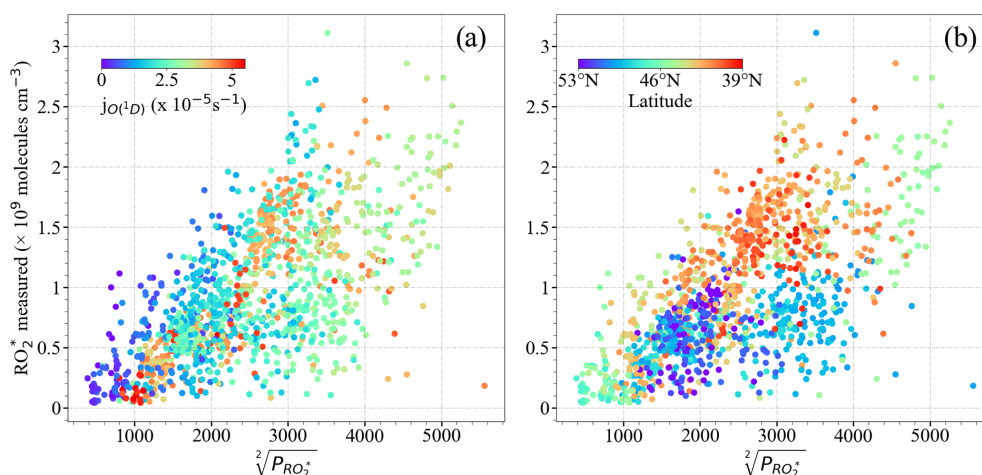


Figure 7. Measured $[\text{RO}_2^*]$ versus calculated $\sqrt{P_{\text{RO}_2^*}}$ colour-coded for values of (a) $j_{\text{O}(1\text{D})}$ and (b) latitude.

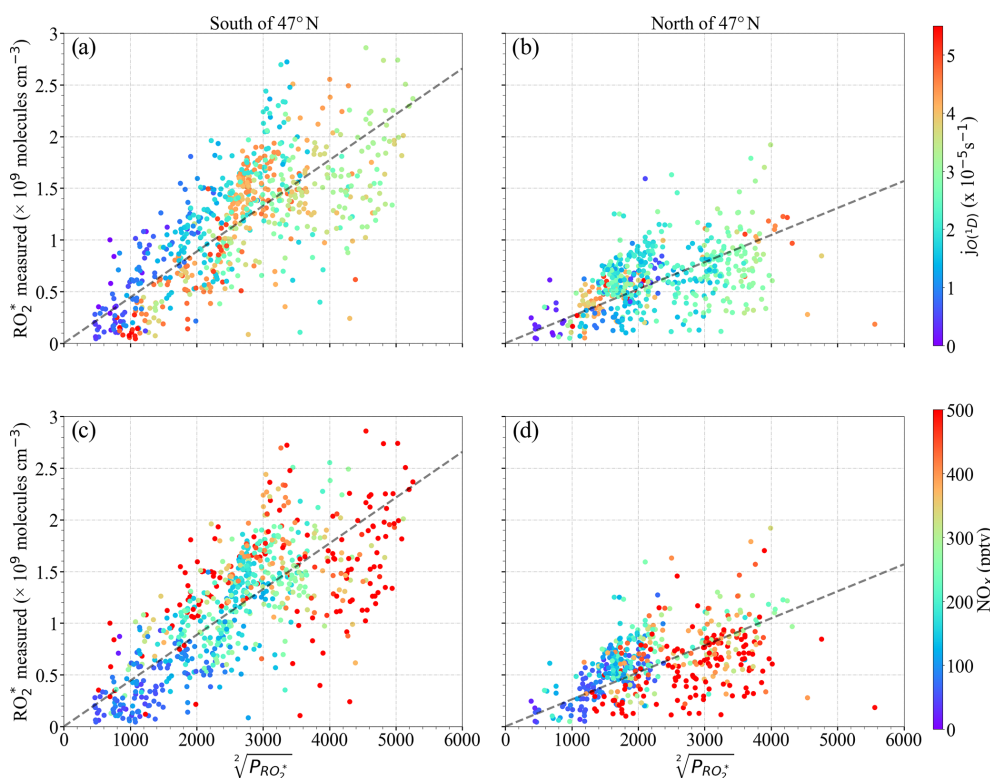


Figure 8. Measured $[\text{RO}_2^*]$ versus $\sqrt{P_{\text{RO}_2^*}}$ for the following latitudes: (a, c) south of 47°N and (b, d) north of 47°N . Note that (a) and (b) are colour-coded with $j_{\text{O}(1\text{D})}$; (c) and (d) are colour-coded with the NO_x mixing ratio. The dashed lines indicate the linear fit for visual support.

tion of altitude. The data are classified into three groups according to the rate of destruction of RO_2^* mixing ratio: $D_{\text{RO}_2^*} < 0.01 \text{ pptv s}^{-1}$ (a), $0.01 < D_{\text{RO}_2^*} < 0.9 \text{ pptv s}^{-1}$ (b), and $D_{\text{RO}_2^*} > 0.9 \text{ pptv s}^{-1}$ (c) to show the lowest, most common, and highest ranges, respectively, encountered during the EMeRGe campaign. For 90% of the measurements,

$0.01 < D_{\text{RO}_2^*} < 0.9 \text{ pptv s}^{-1}$ applies, while the rest of the data are equally distributed in the other two $D_{\text{RO}_2^*}$ ranges. The data in each group are always binned over 500 m when available.

As can be seen in Fig. 9, the $\pm 1\sigma$ standard deviation of the obtained bins is very high. In spite of this, the $\text{HO}_2\text{-CH}_3\text{O}_2$ and $\text{HO}_2\text{-HO}_2$ reactions seem to dominate the radical de-

struction processes in the air masses probed. Their combined contribution is $> 70\%$ in all the cases except in the 1000 m bin of $D_{RO_2^*} > 0.9$ pptv s^{-1} . Other significant radical losses occur through the HONO and HNO₃ formation. The contribution of the CH₃O₂+CH₃O₂ reaction to the total RO₂^{*} destruction rate is $< 5\%$.

Since Eq. (6) is quadratic in [RO₂^{*}], it can be solved for [RO₂^{*}]_c, where “c” stands for calculated, as

$$[RO_2^*]_c = \frac{-(-L_{RO_2^*}) - \sqrt{L_{RO_2^*}^2 - 4(-2k_{RO_2^*})P_{RO_2^*}}}{2(-2k_{RO_2^*})}, \quad (9)$$

where

$$\begin{aligned} k_{RO_2^*} &= (k_{16a}(1-\delta)^2 + k_{15}\delta(1-\delta) + k_{14}\delta^2), \\ L_{RO_2^*} &= (\delta(k_{23}[NO] + k_{24}[O_3])\rho), \\ P_{RO_2^*} &= (2j_1[O_3]\beta + j_3[HONO])(1-\rho) \\ &\quad + 2j_8[HCHO] + 2j_9[CH_3CHO] \\ &\quad + 2(j_{10a} + j_{10b})[CH_3C(O)CH_3] + 2j_{11}[CHOCHO], \end{aligned}$$

and where $k_{RO_2^*}$ is a weighed rate coefficient of RO₂^{*} self-reactions for a 1 : 1 mixture of HO₂ and CH₃O₂, $L_{RO_2^*}$ comprises the formation of HONO and HNO₃, and $P_{RO_2^*}$ is the gross production of RO₂^{*}.

The second solution of the quadratic equation gives negative values for [RO₂^{*}]_c; therefore, it is assumed to have no physical meaning. A more detailed derivation of Eqs. (6) and (9) are given in the Supplement.

Figure 10 shows the measured RO₂^{*} (hereinafter referred to as RO_{2m}^{*}) mixing ratio versus the calculated RO_{2c}^{*} mixing ratio using Eq. (9). RO_{2m}^{*} and RO_{2c}^{*} are the measured and calculated RO₂^{*} respectively for $\delta = 1$ (i.e. RO₂^{*} = HO₂) and $\delta = 0.5$ (i.e. HO₂ = RO₂^{*}). The eCL values corresponding to $\delta = 1$ and $\delta = 0.5$ used for the RO_{2m}^{*} retrievals were determined in laboratory experiments, as reported by George et al. (2020). The small circles represent 1 min RO_{2m}^{*}, whereas the large circles are the mean of the RO_{2m}^{*} binned over 10 pptv RO_{2c}^{*} intervals. The RO₂^{*} data are colour-coded with the onboard NO measurements. The linear regression slopes are around 0.7 ($R^2 = 0.96$), indicating an overall 25%–30% overestimation of the RO_{2m}^{*}. The y-axis intercept is below the instrumental detection limit for most measurement conditions.

Figure 11 shows the vertical profiles of RO_{2m}^{*} and RO_{2c}^{*} mixing ratios calculated for $\delta = 0.5$, averaged for the EMerGe flights over Europe in 500 m altitude bins. RO_{2c}^{*} seems to overestimate RO_{2m}^{*} for altitudes above 4000 m. As mentioned in Sect. 4.1, the vertical profiles are a composite from averaging flights with legs carried out at different longitudes and latitudes. Therefore, the differences between RO_{2m}^{*} and RO_{2c}^{*} have been studied in more detail with respect to the composition of the individual air masses (see the

RO_{2m}^{*} and RO_{2c}^{*} mixing ratios as a function of latitude and altitude in Fig. S4 in the Supplement).

Figure 12 shows the data for $\delta = 0.5$ colour-coded with NO; NO_x; the sum of HCHO, CH₃CHO, CHOCHO, CH₃OH, and CH₃C(O)CH₃ (from now on referred to as Σ VOCs), as a surrogate for the amount of OVOCs acting as RO₂^{*} precursors; and the Σ VOCs to NO ratio. The largest differences between RO_{2m}^{*} and RO_{2c}^{*} are observed for the bins around 50 pptv. The RO_{2c}^{*} values overestimate the RO_{2m}^{*} mostly for RO_{2m}^{*} < 25 pptv observed above ≈ 4000 m. These air masses are characterised by NO < 50 pptv, Σ VOCs typically below 4 ppbv, high Σ VOCs/NO ratios (> 50), and low insolation conditions (i.e. $j_{O(1D)} < 2 \times 10^{-5} s^{-1}$) (see Fig. S5 in the Supplement). Under these insolation conditions, the radical production rate is expected to be low, and the RO₂^{*}–RO₂^{*} reactions are expected to dominate the RO₂^{*} loss processes. As OH and H₂O₂ were not measured during the EMerGe campaign in Europe, Eq. (9) does not include the loss Reactions (R17) and (R18), which might be significant under such conditions (Tan et al., 2001) and explain the overestimation of RO_{2m}^{*}. This is also the case for the overestimations observed below 40 pptv RO_{2m}^{*} at other altitudes, where NO < 50 pptv but the Σ VOCs/NO ratios remain low. The overestimation may therefore be independent of the Σ VOCs/NO ratios. For NO ≤ 50 pptv, NO₂ ≤ 100 pptv, RO₂^{*} ≤ 40 pptv, and HCHO ≤ 1 ppbv, the rate of Reaction (R17), which forms H₂O and O₂ from OH and HO₂, is about 4 times faster than the rate of the OH oxidation reaction of the dominant OVOCs (Reaction R12) considered in this study or the rate of formation of HONO (Reaction R19).

RO_{2m}^{*} is both underestimated and overestimated for Σ VOCs mixing ratios greater than 7 ppbv. The composition of these air masses is very different, as reflected by the Σ VOCs/NO ratios. This implies that Eq. (9) does not capture the peroxy radical yields adequately from the measured VOCs and OVOC in these cases. The differences between RO_{2m}^{*} and RO_{2c}^{*} may be explained in part by (a) changes in OH yields due to additional VOC oxidation processes, which are not in Eq. (9); (b) RO₂^{*} production from the photolysis of carbonyls, which were not measured; (c) RO₂^{*} production from the ozonolysis of alkenes or unidentified biogenic terpene emissions; and/or (d) overestimation of the loss processes.

In addition, Eq. (9) does not consider the loss of RO₂ through the organic nitrate formation (Reaction R25b), which results in an underestimation of radical loss in the presence of RO₂ with organic groups larger than CH₃. Tan et al. (2019) reported that changing the yields for organic nitrate formation channel in Reaction (R25) from 5% to 20% has a small but notable influence on their experimental budget analysis. Similarly, the RO₂ loss through organic nitrate formation, which is not included in Eq. (9), might explain the

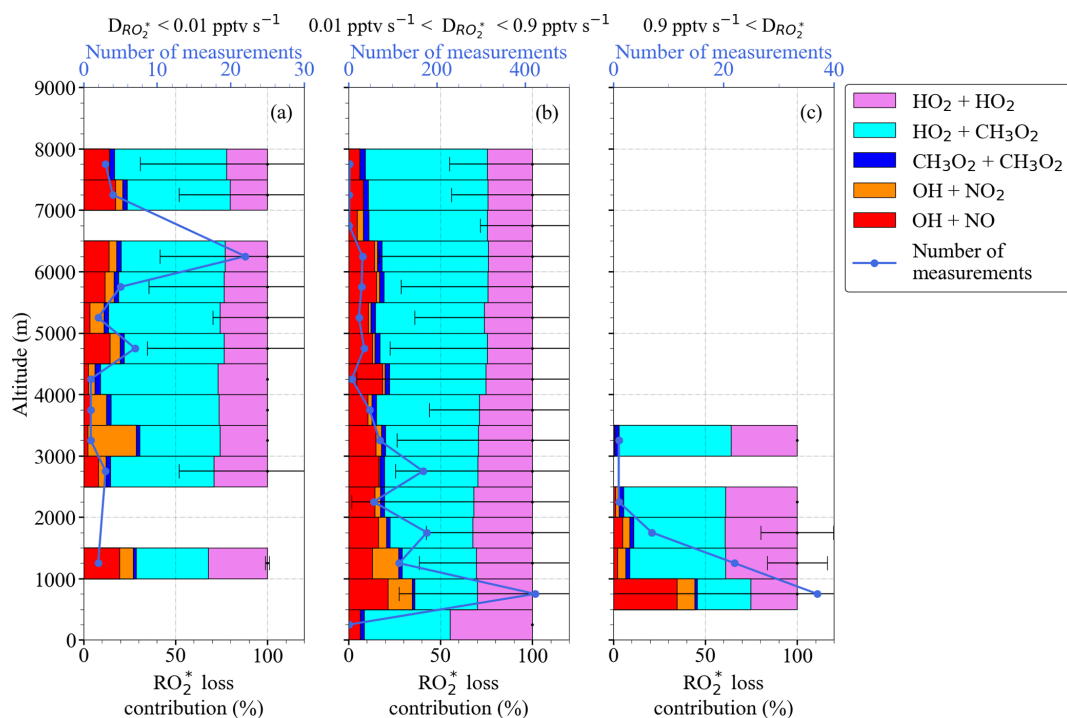


Figure 9. RO_2^* destruction rate ($D_{RO_2^*}$) and fractional contributions from loss reactions in Eq. (6) as a function of altitude for (a) $D_{RO_2^*} < 0.01 \text{ pptv s}^{-1}$, (b) $0.01 \text{ pptv s}^{-1} < D_{RO_2^*} < 0.9 \text{ pptv s}^{-1}$, and (c) $D_{RO_2^*} > 0.9 \text{ pptv s}^{-1}$. Note the different scales in the number of measurements.

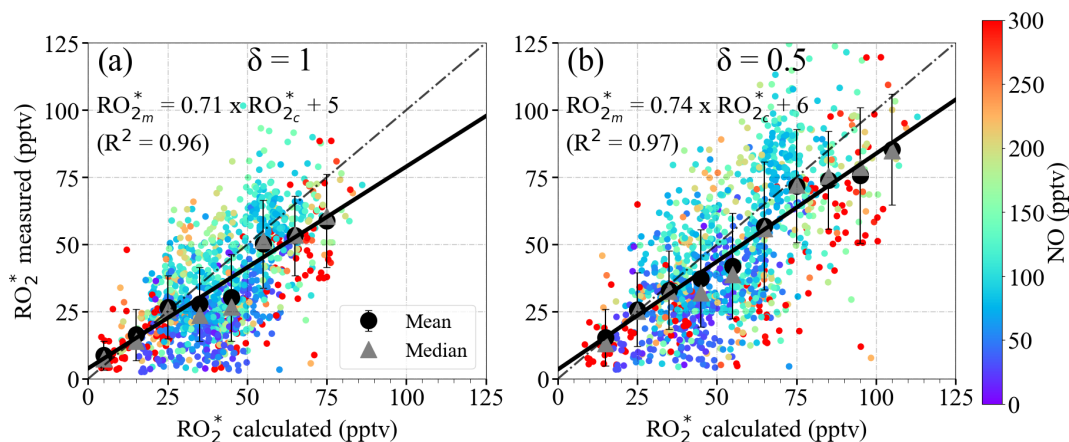


Figure 10. RO_{2m}^* versus RO_{2c}^* using Eq. (9) for (a) $\delta = 1$ and (b) $\delta = 0.5$. The data are colour-coded with the measured NO mixing ratios. The 1 min data (small circles), the mean of the binned RO_{2m}^* over 10 pptv RO_{2c}^* intervals (large circles), and the median of each bin (grey triangles) are shown. The error bars indicate the $\pm 1\sigma$ standard deviation of each bin. The linear regression for the binned values (solid line) and the 1 : 1 relation (dashed line) are also depicted for reference.

RO_{2m}^* overestimations for $\sum \text{VOC} < 2 \text{ ppb}$, $\sum \text{VOCs} / \text{NO} < 20$, and for $\text{NO} > 200 \text{ pptv}$.

Although considered small, the spatial and temporal differences in the in situ measurements of the key trace gases (O_3 , NO, H_2O , CO, CH_4 , VOCs) as compared to those of the remote sensing observations (NO_2 and HONO) used in Eq. (9) may also contribute to the overall spread observed

in Fig. 12. Although the temporal evolution and the amount of the trace gases measured using in situ and remote sensing instruments agree reasonably well, as shown for HCHO in Fig. 13, the remote sensing instruments have, in general, larger air sampling volumes compared to that of in situ instruments. This may occasionally lead to significant differences depending on the location of the pollutant layers

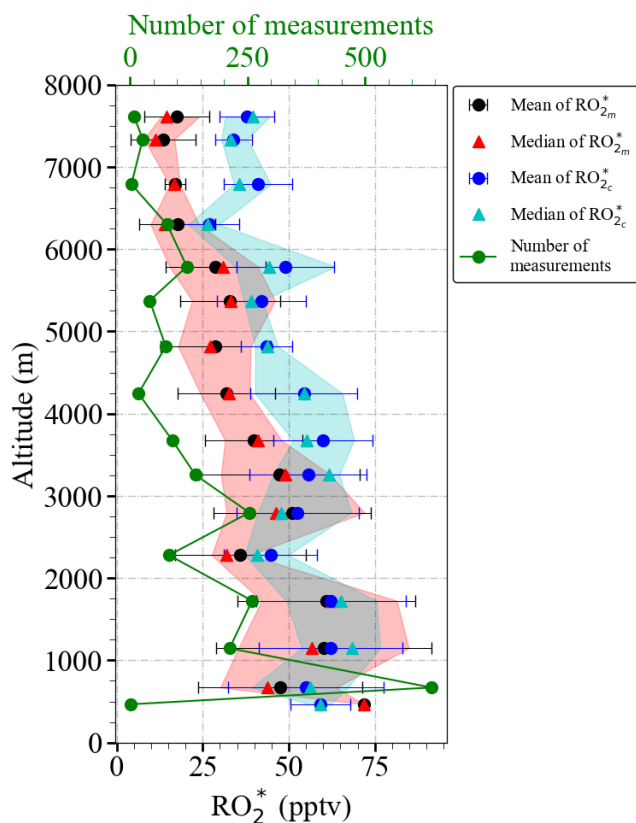


Figure 11. Vertical distribution of the mean RO_{2m}^* and mean RO_{2c}^* using Eq. (9) for $\delta = 0.5$ for the EMeRGe data set in Europe. The measurements are binned over 500 m altitude. The error bars are the $\pm 1\sigma$ standard deviation of each bin. Median values (red and cyan triangles), the interquartile 25%–75% range (red and blue shaded areas), and the number of individual measurements for each bin (in green) are additionally plotted.

with respect to HALO. In addition, PTR-MS measurements of HCHO might include interferences from molecular fragments of other compounds in the sample air (Inomata et al., 2008). Further details about the accuracy and comparability of the onboard instrumentation during the campaign can be found elsewhere (Schumann, 2020).

In summary, apart from the inaccuracies in the reaction rate coefficients, the differences between RO_{2m}^* and RO_{2c}^* might be caused by a combined effect of the limitations of the analytical expression to simulate complex non-linear chemistry and the measurement uncertainties arising from the spatial heterogeneity of the plume for the remote sensing instruments. Consequently, the quantification of limiting factors in Eq. (9) require the analysis of the pollution events encountered along the flights individually.

The ratio of RO_{2m}^* to RO_{2c}^* (RO_{2m}^*/RO_{2c}^*) has been used to assess the applicability of Eq. (9) for the calculation of RO_2^* in the air masses probed. In Fig. 14, the data are colour-coded with respect to RO_{2m}^*/RO_{2c}^* , H_2O , $\Sigma VOCs$, and NO_x . The air masses probed at altitudes above 2000 m

are close to the PSS assumptions used to develop Eq. (9), and consequently, the RO_{2m}^*/RO_{2c}^* ratio remains ≤ 1 . In contrast, RO_{2m}^*/RO_{2c}^* is at its highest value below 2000 m, reaching up to 3. At these altitudes, most of the flights in Europe were carried out in pollution plumes, in which both the amounts of NO_x and RO_2^* precursors are high. The analytical expression does not capture the RO_2^* variations resulting from fast non-linear photochemistry present in these pollution plumes. This is the case for the measurements made between 42 and 46° N in the outflow of the Po Valley and Rome. $\Sigma VOCs > 7$ ppbv and NO_x mixing ratios > 500 pptv indicate high radical precursor loading and relatively fresh emissions. The RO_{2m}^*/RO_{2c}^* is also > 2 in the measurements over the English Channel (between 50 and 52° N) with $\Sigma VOCs$ and NO_x mixing ratios > 7 ppbv and 1000 pptv, respectively.

The applicability of Eq. (9) for calculating the in-flight measurements of RO_2^* along the track of the E-EU-03 flight on 11 July 2017 was studied in more detail. The E-EU-03 flight investigated the outflow of selected MPCs in Italy (i.e. Po Valley and Rome). Consequently, the flight track was routed along the western coast of Italy and included vertical profiling over the Tyrrhenian Sea upwind of Rome (see Fig. S6 in the Supplement). As indicated by $j_{O(1D)}$, in Fig. 15, cloudless conditions dominated throughout the flight track. The RO_{2c}^* values agree reasonably well with RO_{2m}^* throughout this period except in the pollution plume measured from 12:05 to 12:25 UTC. In this plume, CO, NO, NO_2 , HONO, NO_y , and HCHO were 100 ppbv, 180 pptv, 150 pptv, 120 pptv, 1 ppbv and 2 ppbv, respectively. The RO_{2m}^* values are approximately 20% underestimated by RO_{2c}^* during this period. Backward trajectories calculated using FLEXTRA (Stohl et al., 1995; Stohl and Seibert, 1998) indicate the transport of pollution through the Mediterranean mixed with dust plumes originating from Tunisia. The NO mixing ratios observed indicate the proximity to emission sources.

The measurements of VOCs used in Eq. (9) may not be representative of the actual complex VOC composition in the plume measured from 12:05 to 12:25 UTC. Consequently, the RO_2 to HO_2 ratio, the branching ratios, and effective rate coefficients for $RO_2^*-RO_2^*$ reactions might not be well represented in Eq. (9). Taking CH_3O_2 as a surrogate for all RO_2 might lead to uncertainties in the RO_2^* calculations in the presence of OVOCs with larger organic chains. On the experimental side, changes in the HO_2 to RO_2 ratio affect the accuracy of the PerCEAS retrieval of the total sum of radicals. As noted in Sect. 3, in this study $RO_2^* = HO_2 + 0.65 \times RO_2$, and the eCL is determined for a 1 : 1 mixture of $HO_2 : CH_3O_2$ (i.e. $\delta = 0.5$ is used for the RO_2^* retrieval). However, the HO_2 to CH_3O_2 ratio is not expected to remain constant in all the air masses probed. For a 3 : 1 ratio of $HO_2 : RO_2$, the RO_{2m}^* would decrease by 10%. Similarly, a $HO_2 : RO_2$ ratio of 1 : 3 would lead to an increase of 10% in the reported RO_{2m}^* . This uncertainty is well below the in-flight uncertainty of the PerCEAS instrument indicated by the error bars in Fig. 14

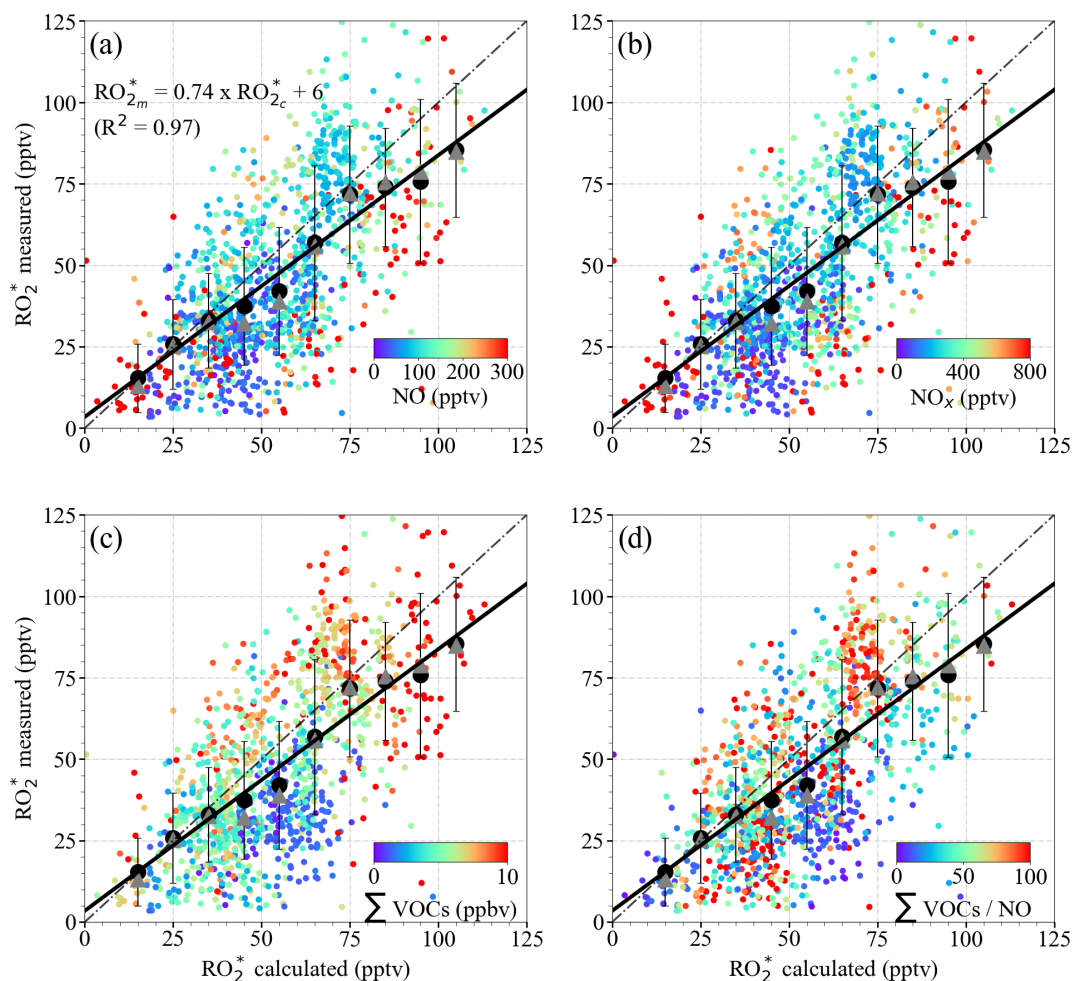


Figure 12. RO_{2m}^* versus RO_{2c}^* using Eq. (9) for $\delta = 0.5$ colour-coded with the measured (a) NO mixing ratio; (b) NO_x mixing ratio; (c) $\Sigma VOCs$ mixing ratio, where $\Sigma VOCs = HCHO + CH_3CHO + (CHO)_2 + CH_3OH + CH_3C(O)CH_3$; and (d) $\Sigma VOCs / NO$ ratio. The 1 min data (small circles), the mean of the binned RO_{2m}^* over 10 pptv RO_{2c}^* intervals (large circles), and the median of each bin (triangles) are shown. The error bars represent the $\pm 1\sigma$ standard deviation of each bin. The linear regression for the binned values (solid line) and the 1 : 1 relationship (dashed line) are plotted for reference.

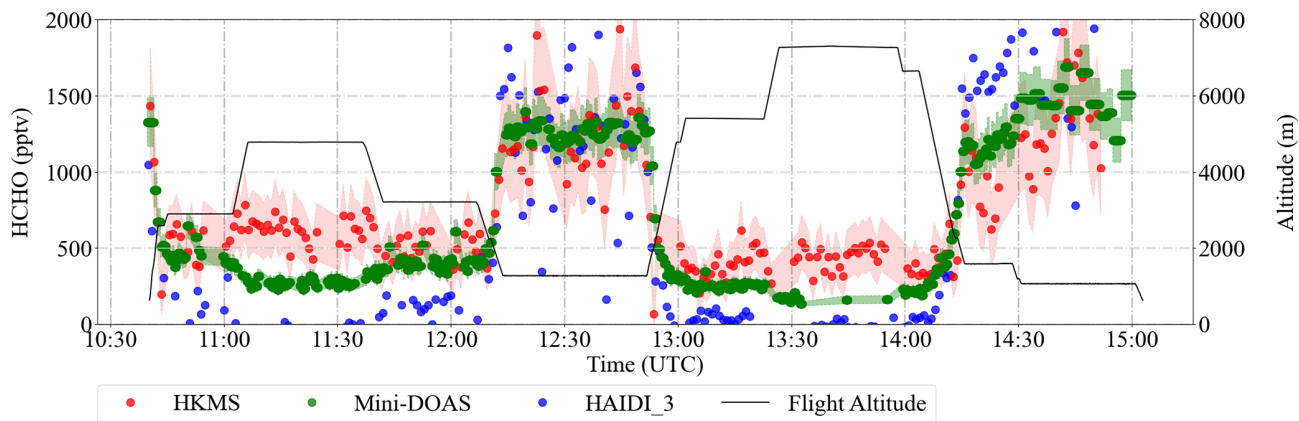


Figure 13. An example of the time series of the measured HCHO mixing ratios retrieved from the remote sensing (HAIDI in blue and miniDOAS in green) and in situ (HKMS in red) instruments during the E-EU-04 flight on 14 July 2017. The shaded region shows $\pm 1\sigma$ uncertainties of the HKMS and miniDOAS instruments. The flight altitude is depicted in black.

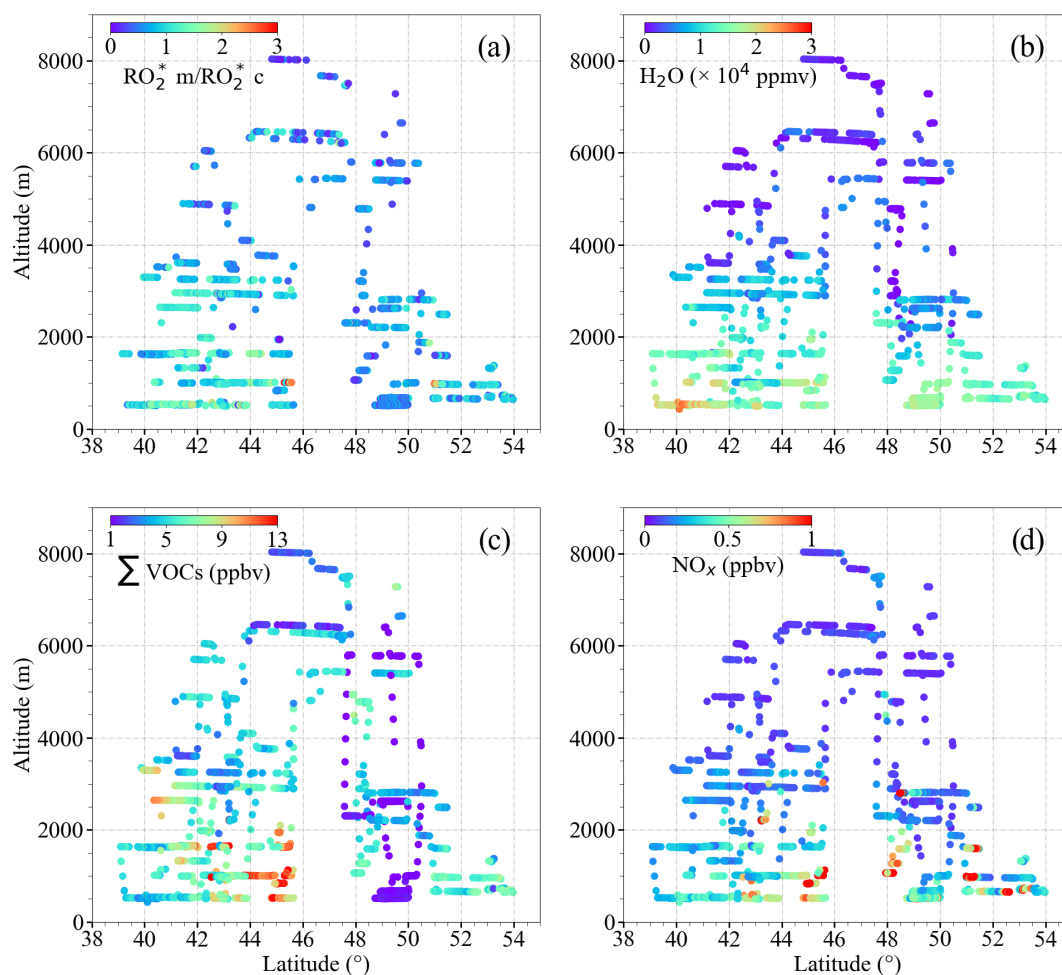


Figure 14. Plots of (a) the ratio of $\text{RO}_{2\text{m}}^*$ to $\text{RO}_{2\text{c}}^*$ ($\text{RO}_{2\text{m}}^*/\text{RO}_{2\text{c}}^*$) assuming that $\delta = 0.5$; (b) H_2O ; (c) $\sum \text{VOCs}$; (d) NO_x as a function of latitude and altitude for the EMerGe measurements in Europe.

(George et al., 2020) and cannot account for the overall underestimation. However, it might reduce the differences observed between $\text{RO}_{2\text{m}}^*$ and $\text{RO}_{2\text{c}}^*$ in particular cases. A complete explanation of the variability of RO_2^* in the pollution plumes measured within the campaign in Europe is beyond the scope of this analysis and requires an investigation by high-resolution chemical models.

4.4 Comparison of results with other studies

4.4.1 RO_2^* production rate

Cantrell et al. (2003b) proposed that the production of RO_2^* , $P_{\text{RO}_2^*}$, is equal to the sum of two terms representing $\text{RO}_2^*-\text{RO}_2^*$ reactions and the $\text{RO}_2^*-\text{NO}_x$ reactions in the troposphere. As a result of this assumption, these authors describe the relationship between HO_2 , RO_2 , $P_{\text{RO}_2^*}$, and NO_x as

$$P_{\text{RO}_2^*} = k_{\text{RR}}[\text{HO}_2 + \text{RO}_2]^2 + k_{\text{RN}}[\text{HO}_2 + \text{RO}_2][\text{NO}_x], \quad (10)$$

where k_{RR} and k_{RN} refer to effective rate coefficients for $\text{RO}_2^*-\text{RO}_2^*$ and $\text{RO}_2^*-\text{NO}_x$ reactions, respectively, and are calculated as fit parameters. Solving Eq. (10) for $[\text{HO}_2 + \text{RO}_2]^2$ leads to

$$[\text{HO}_2 + \text{RO}_2] = \sqrt{A + B^2} - B, \quad (11)$$

where $A = \frac{P_{\text{RO}_2^*}}{k_{\text{RR}}}$ and where $B = \frac{k_{\text{RN}}[\text{NO}_x]}{2k_{\text{RR}}}$. For low NO_x and/or high $P_{\text{RO}_2^*}$, B becomes negligible compared to A . Then $[\text{HO}_2 + \text{RO}_2]$ approaches \sqrt{A} and is independent of NO_x . For high NO_x and/or low $P_{\text{RO}_2^*}$, $[\text{HO}_2 + \text{RO}_2]$ approaches zero.

The $\text{RO}_{2\text{m}}^*$ and $\text{RO}_{2\text{c}}^*$ values for the EMerGe observations in Europe, binned in $0.1 \text{ pptv s}^{-1} P_{\text{RO}_2^*}$ intervals, were fitted according to the procedure by Cantrell et al. (2003b), and the results are shown in Fig. 16. The obtained fit parameters for Fig. 16a and b are $k_{\text{RR}} = 7 \times 10^{-5}$ and $k_{\text{RN}} = 9 \times 10^{-6}$. The RO_2^* calculated by Eq. (9) appears to be close to the linear function of the NO_x measured. Similar to the results of the study by Cantrell et al. (2003b), a decrease in RO_2^* with NO_x

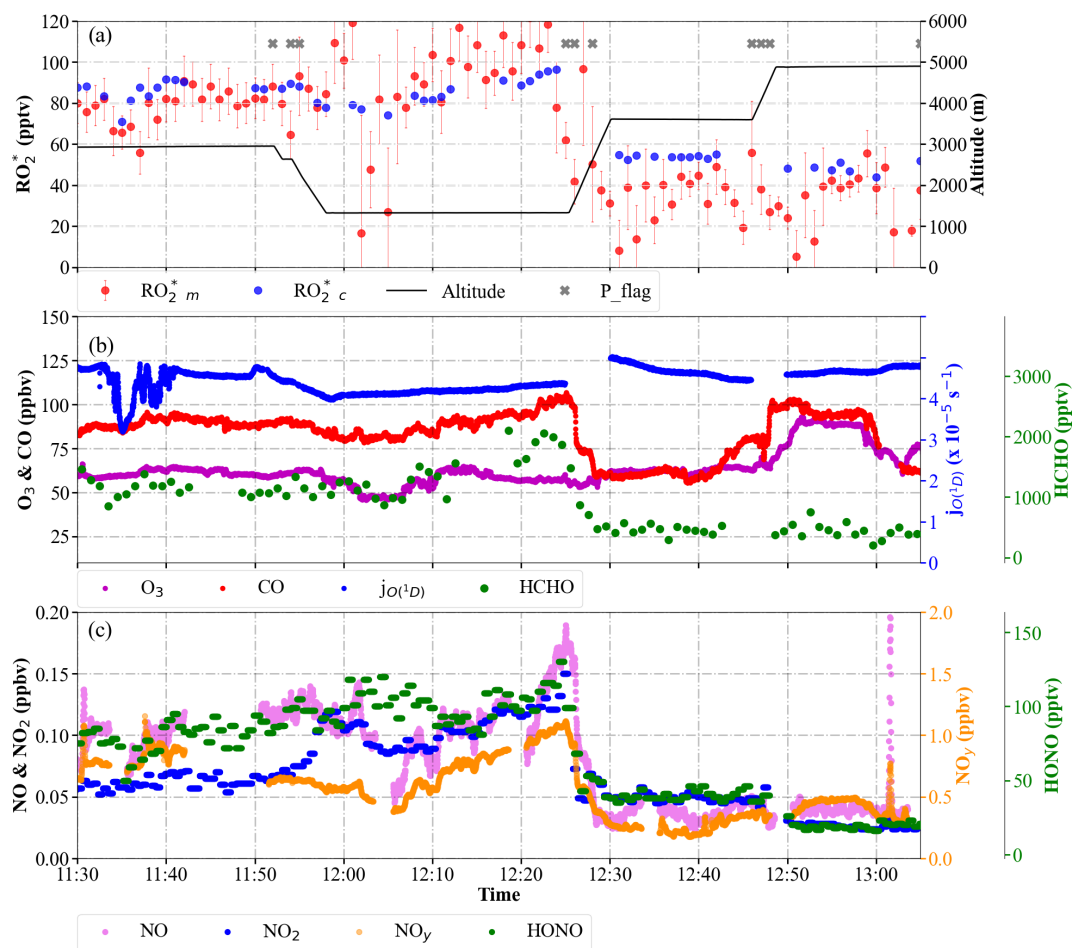


Figure 15. Temporal variation of $\text{RO}_2^*_{\text{m}}$ and $\text{RO}_2^*_{\text{c}}$, selected radical precursors, and $j_{\text{O}(^1\text{D})}$ along the E-EU-03 flight track: (a) $\text{RO}_2^*_{\text{m}}$ and $\text{RO}_2^*_{\text{c}}$ mixing ratios. The flight altitude is indicated in black. The P_flag indicates RO_2^* measurements affected by dynamical pressure variation in the inlet; (b) O_3 , CO, HCHO mixing ratios, and $j_{\text{O}(^1\text{D})}$; (c) NO, NO_2 , NO_y , and HONO mixing ratios.

is identified for $\text{NO}_x > 1000$ pptv. $\text{RO}_2^*_{\text{c}}$ does not show any decrease with increase in NO_x for $P_{\text{RO}_2^*} \geq 0.7$ pptv s^{-1} . This might be explained by the underestimation of radical losses through organic nitrate formation in Eq. (9) as explained in Sect. 4.3.

Despite the low agreement of the fitted lines with the $\text{RO}_2^*_{\text{m}}$, a decrease in $\text{RO}_2^*_{\text{m}}$ as a function of NO_x is still observed. The disagreement between $\text{RO}_2^*_{\text{m}}$ and the curves estimated using Eq. (11) implies that the simplified Eq. (10) from Cantrell et al. (2003b) is insufficient to adequately describe the chemical and physical processes occurring in the air masses probed. Part of the disagreement might arise from missing terms in the $P_{\text{RO}_2^*}$ calculated using Eq. (3) or inaccuracies related to the NO to NO_2 ratio in the air mass, which are more evident at higher $P_{\text{RO}_2^*}$. As expected, the ratio of calculated $[\text{RO}_2^*_{\text{c}}]$ to $\sqrt{P_{\text{RO}_2^*}}$ has a negative linear dependence on the measured $[\text{NO}_x]$ (see Fig. 16c). The comparable relationship of $\frac{\text{RO}_2^*_{\text{m}}}{\sqrt{P_{\text{RO}_2^*}}}$ to $[\text{NO}_x]$ is not linear for $\text{NO}_x < 100$ pptv

approximately (see Fig. 16d). This indicates that the simplified approach by Cantrell et al. (2003b) is not applicable to the more complex non-linear processes involved in the air masses investigated within EMERGE.

4.4.2 O_3 production rate

The O_3 production rate (P_{O_3}) is calculated from the EMERGE Europe data set using the reaction of RO_2^* with NO in a similar manner to that used in previous studies of photochemical processes in urban environments (e.g. Kleinman et al., 1995; Volz-Thomas et al., 2003; Mihelcic et al., 2003; Cantrell et al., 2003b; and references herein).

$$P_{\text{O}_3} = k_{\text{RO}_2^*+\text{NO}} [\text{RO}_2^*] [\text{NO}], \quad (12)$$

where $k_{\text{RO}_2^*+\text{NO}}$ is taken as the average of $k_{\text{HO}_2+\text{NO}}$ and $k_{\text{CH}_3\text{O}_2+\text{NO}}$.

Figure 17 shows the mean P_{O_3} calculated using Eq. (12) from $\text{RO}_2^*_{\text{m}}$ and $\text{RO}_2^*_{\text{c}}$ as a function of NO. The measured

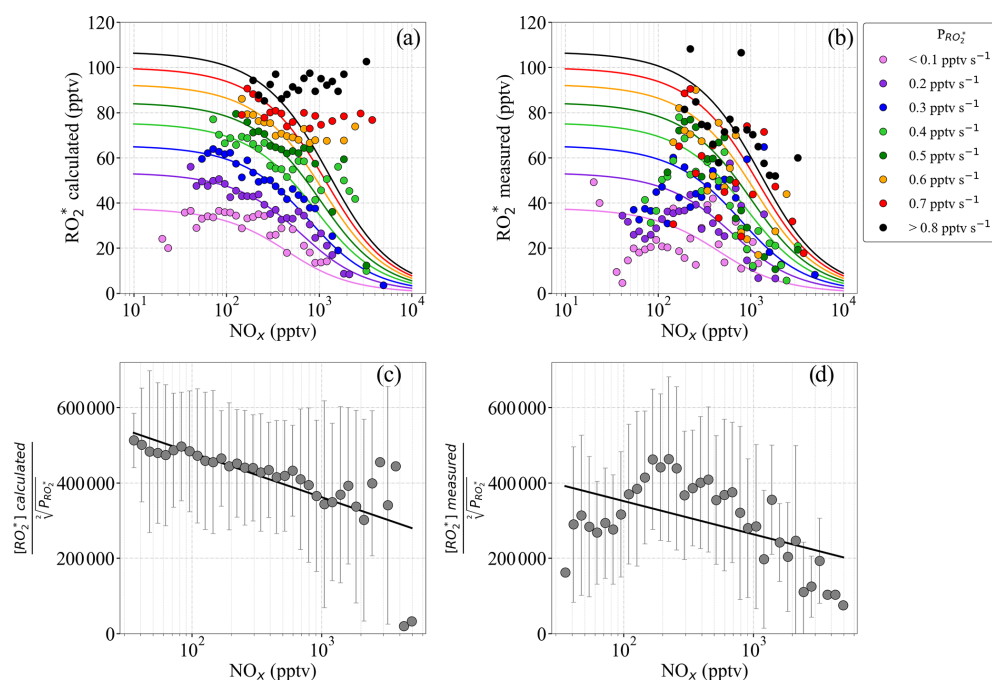


Figure 16. (a) RO_{2c}^* binned into $P_{RO_2^*}$ intervals of 0.1 pptv s^{-1} versus binned NO_x ; (b) RO_{2m}^* binned into $P_{RO_2^*}$ intervals of 0.1 pptv s^{-1} versus binned NO_x ; (c) ratio of $[RO_{2c}^*]$ to $\sqrt{P_{RO_2^*}}$ versus NO_x ; and (d) $[RO_{2m}^*]$ to $\sqrt{P_{RO_2^*}}$ ratio versus NO_x . The data in panels (a) and (b) are assigned different colours, as a function of the radical production rate interval. The NO_x observations are binned into 50 equidistant intervals on a logarithmic scale. The solid lines in panels (a) and (b) are the least square fits, obtained using Eq. (10). In panels (c) and (d), the ratios of $[RO_{2c}^*]$ to $\sqrt{P_{RO_2^*}}$ and $[RO_{2m}^*]$ to $\sqrt{P_{RO_2^*}}$ are binned into 50 NO_x intervals equidistant on the logarithmic scale from 10 to 10 000 pptv. Error bars indicate the $\pm 1\sigma$ standard deviation for the distribution in each bin.

NO mixing ratios are binned into 50 bins. The bin size increases with NO to keep the points equidistant on the logarithmic scale. The calculated P_{O_3} values for the RO_{2m}^* and RO_{2c}^* agree well within the standard deviation of the bins.

Similar P_{O_3} values have been reported for ground-based measurements in polluted areas such as Wangdu (Tan et al., 2017) and Beijing (Whalley et al., 2021) and similar ranges of peroxy radicals and NO mixing ratios. In previous work, Whalley et al. (2018) calculated P_{O_3} to be about an order of magnitude lower than that found in this study from observations in central London for about an order of magnitude lower amount of $HO_2 + RO_2$. For $NO > 1 \text{ ppbv}$, the P_{O_3} estimated from the measurement of HO_2 and RO_2 or from the assumptions of an HO_2 to RO_2 ratio were underestimated by the models in other studies in the urban atmosphere (e.g. Martinez et al., 2003; Ren et al., 2003; Kanaya et al., 2008; Mao et al., 2010; Kanaya et al., 2012; Ren et al., 2013; Brune et al., 2016; Griffith et al., 2016). This behaviour is generally attributed to an underestimate of the concentration of RO_2 with a large organic group, which likely undergoes multiple bimolecular reactions with NO before forming an HO_2 radical.

During the EMeRGe campaign in Europe, the NO mixing ratios were $< 1 \text{ ppbv}$ (approximately

$< 3 \times 10^{10} \text{ molecules cm}^{-3}$). The ozone production rates obtained for both RO_{2m}^* and RO_{2c}^* are in reasonable agreement with other modelling studies in urban environments where the mixing ratio of NO is $< 1 \text{ ppbv}$ (Tan et al., 2017; Whalley et al., 2021).

5 Summary and conclusions

This study exploits the airborne measurements of various atmospheric constituents on board HALO over Europe in summer 2017 to investigate radical photochemistry in the probed air masses. RO_2^* values are calculated by assuming a photo-stationary steady state (PSS) of RO_2^* and are compared with the actual measurements. The calculation is constrained by the simultaneous airborne measurements of radical precursors, photolysis frequencies, and reactants of RO_2^* such as NO_x and O_3 . The calculated radical production rates, $P_{RO_2^*}$, do not significantly vary with altitude in the air masses investigated as the increase in the photolysis frequencies as a function of altitude is concurrent with decreases in precursor concentrations.

The significance and the importance of selected initiating and terminating processes in the RO_2^* chemistry are investigated by gradually increasing the complexity of the ana-

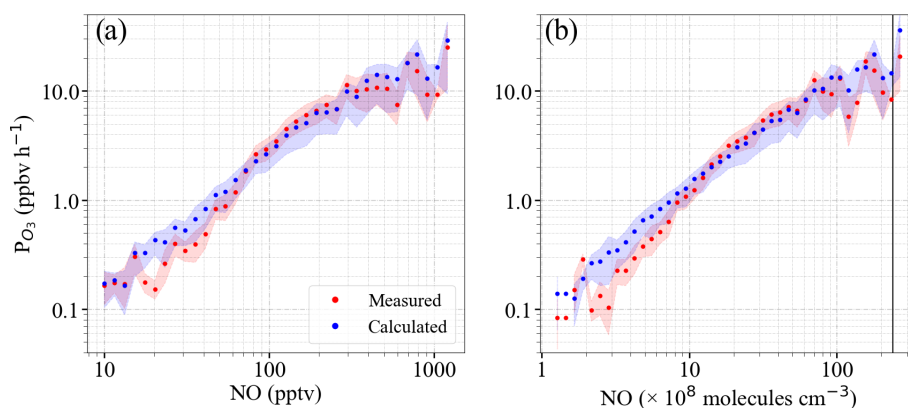


Figure 17. Calculated O₃ production rate (P_{O_3}) determined using RO_{2m}^{*} (red dots) and RO_{2c}^{*} (blue dots) as a function of the following: (a) NO mixing ratio and (b) NO number density. The 1 min measurements are binned into 50 bins of NO equidistant on the logarithmic scale for panel (a) from 10 to 10 000 pptv and for panel (b) from 5×10^7 to 3.5×10^{10} molecules cm⁻³, respectively. The shaded area shows the $\pm 1\sigma$ standard deviation of each bin. To facilitate comparison with ground-based measurements, the black line plotted in panel (b) is the number density corresponding to 1 ppbv NO at 1000 mbar and 25 °C.

lytical expression. The agreement of the calculations with the measurements over a wide range of chemical composition and insolation conditions improves when the analytical expression is extended to account for effective radical yields from VOC oxidation and radical losses through nitrate and nitrite formation. The RO₂^{*} measured is usually overestimated when NO is < 50 pptv in the air probed. This behaviour might be explained by RO₂^{*} loss processes involving reactions with OH (e.g. the reaction of HO₂ with OH but possibly to a lesser extent the three-body reaction of OH with itself to make H₂O₂). These reactions may become significant RO₂^{*} loss processes at low NO concentrations as measured during the campaign but are excluded from the analytical expression, which is constrained by onboard measurements. Similarly, the RO₂ loss through organic nitrate is also excluded from the analytical expression. These reactions may become significant RO₂^{*} loss processes in the presence of RO₂ with organic groups larger than CH₃. This might explain some of the RO₂^{*} overestimations by the analytical expression observed for NO > 200 pptv.

The RO₂^{*} calculated under assumption of a photostationary state mostly underestimated the RO₂^{*} measured in polluted plumes of urban origin at altitudes below 2000 m. Changes in the HO₂ to RO₂ ratios in different plumes can account for the disagreement in particular cases. In pollution plumes with the sum of the OVOCs measured mixing ratios being higher than 7 ppbv approximately, the underestimation of the measurements can reach up to 80 %. In these plumes, the oxidation and/or photolysis of VOCs, which were not measured, and the ozonolysis of alkenes might be significant sources of RO₂^{*}, limiting the accuracy of the analytical expression. More information about peroxy radical speciation and VOC partitioning is required to better describe the fast photochemistry in these pollution plumes.

However, the analytical expression developed is robust enough to simulate the radical chemistry in most of the conditions in the free troposphere encountered during EMerGe in Europe. Speciated radical and VOC measurements in future campaigns would facilitate the estimation of radical loss reactions in air masses having NO < 50 pptv and improve radical production rate estimations in pollution plumes having a high amount of VOCs, where non-linear complex chemistry is involved. Comparing RO₂^{*} measurements with RO₂^{*} calculations from the analytical expression helps to identify different chemical and physical regimes, which can be used to constrain future model studies.

The calculated O₃ production rates for NO < 1 ppbv are in the same order of magnitude as those previously reported for urban environments. This indicates that the selected RO₂^{*} production and loss processes and observations of the radical precursors on board are, to a good approximation, adequate for the estimation of the O₃ production in the measured air masses in the free troposphere over Europe.

Data availability. The EMerGe data are available at the HALO database (<https://doi.org/10.17616/R39Q0T>, re3data.org, 2022) and can be accessed upon registration. Further data can be made available upon request to the corresponding author.

Supplement. The supplement related to this article is available online at: <https://doi.org/10.5194/acp-23-7799-2023-supplement>.

Author contributions. MG, VN, and YL undertook the RO₂^{*} measurements, flying as key scientists on board HALO. VN led the deployment of PerCEAS in the HALO aircraft. MG led the analysis of the PerCEAS measurements and prepared the manuscript with contributions from all co-authors. MDAH and JPB initiated the

EMeRGe research project and consortium, acted as co-principal and principal investigators, and participated in the measurement campaigns. They developed the overarching EMeRGe scientific objectives and the required measurement portfolio, directed the EMeRGe research campaigns, and participated in the data analysis presented. AZ, BB, BS, EF, FO, FK, HS, HZ, KB, KP, and TH have contributed by providing their measurements made on board HALO during the campaign and participated in the discussion of results.

Competing interests. The contact author has declared that none of the authors has any competing interests.

Disclaimer. Publisher's note: Copernicus Publications remains neutral with regard to jurisdictional claims in published maps and institutional affiliations.

Special issue statement. This article is part of the special issue "Effect of Megacities on the Transport and Transformation of Pollutants at Regional and Global Scales (EMeRGe) (ACP/AMT inter-journal SI)". It is not associated with a conference.

Acknowledgements. The authors thank the DLRFX and HALO EMeRGe teams for the HALO flight organisation and implementation. Special thanks are given to Lisa Kaser, Frank Probst, Michael Großrubatscher, Stefan Grillenbeck, and Marc Puskeiler for flight coordination and planning; to Alexander Wolf and Thomas Leder, the flight engineers; and to the BAHAMAS team. The authors also thank enviscope GmbH, in particular Nicole Brehm and Rolf Maser, for the support during the integration and preparation phase of the IOP in Europe.

Midhun George, M. Dolores Andrés Hernández, Vladyslav Nenakhov, Yangzhuoran Liu, and John Phillip Burrows thank Wilke Thomssen for support during the preparation and integration phases of EMeRGe and Heiko Schellhorn for continuous technical support and retrieval of model data during the campaigns.

Financial support. The study was funded in part by the German Research Foundation (Deutsche Forschungsgemeinschaft; DFG) HALO-SPP 1294, as well as the University of Bremen and the State of Bremen, IPA, DLR, Oberpfaffenhofen, Germany. The contributions from Benjamin Schreiner, Flora Kluge, and Klaus Pfeilsticker were supported via the DFG (grant nos. PF 384/16, PF 384/17 and PF 384/19). KB was granted funding via the DFG (grant no. PI 193/21-1) and received additional financial from the Heidelberg Graduate School for Physics. Eric Förster was supported via the DFG (grant no. NE 2150/1-1) and received additional financial support from the Karlsruhe Institute of Technology. Midhun George, Yangzhuoran Liu, Maria Dolores Andrés Hernández, and John Philip Burrows received financial support from the University of Bremen.

The article processing charges for this open-access publication were covered by the University of Bremen.

Review statement. This paper was edited by Barbara Ervens and Nga Lee Ng and reviewed by four anonymous referees.

References

- Andrés-Hernández, M. D., Kartal, D., Reichert, L., Burrows, J. P., Meyer Arnek, J., Lichtenstern, M., Stock, P., and Schlager, H.: Peroxy radical observations over West Africa during AMMA 2006: photochemical activity in the outflow of convective systems, *Atmos. Chem. Phys.*, 9, 3681–3695, <https://doi.org/10.5194/acp-9-3681-2009>, 2009.
- Andrés Hernández, M. D., Hilboll, A., Ziereis, H., Förster, E., Krüger, O. O., Kaiser, K., Schneider, J., Barnaba, F., Vrekoussis, M., Schmidt, J., Huntrieser, H., Blechschmidt, A.-M., George, M., Nenakhov, V., Harlass, T., Holanda, B. A., Wolf, J., Eirenschmalz, L., Krebsbach, M., Pöhlker, M. L., Kalisz Hedegaard, A. B., Mei, L., Pfeilsticker, K., Liu, Y., Koppmann, R., Schlager, H., Bohn, B., Schumann, U., Richter, A., Schreiner, B., Sauer, D., Baumann, R., Mertens, M., Jöckel, P., Kilian, M., Stratmann, G., Pöhlker, C., Campanelli, M., Pandolfi, M., Sicard, M., Gómez-Amo, J. L., Pujadas, M., Bigge, K., Kluge, F., Schwarz, A., Daskalakis, N., Walter, D., Zahn, A., Pöschl, U., Bönisch, H., Borrmann, S., Platt, U., and Burrows, J. P.: Overview: On the transport and transformation of pollutants in the outflow of major population centres – observational data from the EMeRGe European intensive operational period in summer 2017, *Atmos. Chem. Phys.*, 22, 5877–5924, <https://doi.org/10.5194/acp-22-5877-2022>, 2022.
- Bohn, B. and Lohse, I.: Calibration and evaluation of CCD spectroradiometers for ground-based and airborne measurements of spectral actinic flux densities, *Atmos. Meas. Tech.*, 10, 3151–3174, <https://doi.org/10.5194/amt-10-3151-2017>, 2017.
- Brito, J. and Zahn, A.: An unheated permeation device for calibrating atmospheric VOC measurements, *Atmos. Meas. Tech.*, 4, 2143–2152, <https://doi.org/10.5194/amt-4-2143-2011>, 2011.
- Brune, W. H., Baier, B. C., Thomas, J., Ren, X., Cohen, R. C., Pusede, S. E., Browne, E. C., Goldstein, A. H., Gentner, D. R., Keutsch, F. N., Thornton, J. A., Harrold, S., Lopez-Hilfiker, F. D., and Wennberg, P. O.: Ozone production chemistry in the presence of urban plumes, *Faraday Discuss.*, 189, 169–189, <https://doi.org/10.1039/c5fd00204d>, 2016.
- Burkholder, J. B., Sander, S. P., Abbatt, J., Barker, J. R., Cappa, C., Crouse, J. D., Dibble, T. S., Huie, R. E., Kolb, C. E., Kurylo, M. J., Orkin, V. L., Wilmouth, D. M., and Wine P. H.: Chemical Kinetics and Photochemical Data for Use in Atmospheric Studies, Evaluation No. 19, JPL Publication 19-5, Jet Propulsion Laboratory, Pasadena, <http://jpldataeval.jpl.nasa.gov> (last access: 29 June 2023), 2019.
- Cantrell, C. A., Shetter, R. E., Calvert, J. G., Eisele, F. L., Williams, E., Baumann, K., Brune, W. H., Stevens, P. S., and Mather J. H.: Peroxy radicals from photostationary state deviations and steady state calculations during the Tropospheric OH Photochemistry Experiment at Idaho Hill, Colorado, 1993, *J. Geophys. Res.*, 102, 6369, <https://doi.org/10.1029/96JD01703>, 1997.
- Cantrell, C. A., Edwards, G. D., Stephens, S., Mauldin, L., Kosciuch, E., Zondlo, M., and Eisele, F.: Peroxy radical observations using chemical ionisation mass spectrometry during TOPSE, *J. Geophys. Res.*, 108, 8381, <https://doi.org/10.1029/2002JD002715>, 2003a.

- Cantrell, C. A., Edwards, G. D., Stephens, S., Mauldin, R. L., Zondlo, M. A., Kosciuch, E., Eisele, F. L., Shetter, R. E., Lefer, B. L., Hall, S., Flocke, F., Weinheimer, A., Fried, A., Apel, E., Kondo, Y., Blake, D. R., Blake, N. J., Simpson, I. J., Bandy, A. R., Thornton, D. C., Heikes, B. G., Singh, H. B., Brune, W. H., Harder, H., Martinez, M., Jacob, D. J., Avery, M. A., Barrick, J. D., Sachse, G. W., Olson, J. R., Crawford, J. H., and Clarke, A. D.: Peroxy radical behaviour during the Transport and Chemical Evolution over the Pacific (TRACE-P) campaign as measured aboard the NASA -3B aircraft, *J. Geophys. Res.*, 108, 8797, <https://doi.org/10.1029/2003JD003674>, 2003b.
- Carpenter, L. J., Clemitshaw, K. C., Burgess, R. A., Penkett, S. A., Cape, J. N., and McFadyen, G. C.: Investigation and evaluation of the NO_x/O_3 photochemical steady state, *Atmos. Environ.*, 32, 3353–3365, [https://doi.org/10.1016/S1352-2310\(97\)00416-0](https://doi.org/10.1016/S1352-2310(97)00416-0), 1998.
- Chen, H., Winderlich, J., Gerbig, C., Hofer, A., Rella, C. W., Crosson, E. R., Van Pelt, A. D., Steinbach, J., Kolle, O., Beck, V., Daube, B. C., Gottlieb, E. W., Chow, V. Y., Santoni, G. W., and Wofsy, S. C.: High-accuracy continuous airborne measurements of greenhouse gases (CO_2 and CH_4) using the cavity ring-down spectroscopy (CRDS) technique, *Atmos. Meas. Tech.*, 3, 375–386, <https://doi.org/10.5194/amt-3-375-2010>, 2010.
- Crawford, J., Davis, D., Olson, J., Chen, G., Liu, S., Gregory, G., Barrick, J., Sachse, G., Sandholm, S., Heikes, B., Singh, H., and Blake, D.: Assessment of upper tropospheric HO_x sources over the tropical Pacific based on NASA GTE/PEM data: Net effect on HO_x and other photochemical parameters, *J. Geophys. Res.*, 104, 16255–16273, <https://doi.org/10.1029/1999JD900106>, 1999.
- Elshorbany, Y. F., Kleffmann, J., Hofzumahaus, A., Kurtenbach, R., Wiesen, P., Brauers, T., Bohn, B., Dorn, H.-P., Fuchs, H., Holland, F., Rohrer, F., Tillmann, R., Wegener, R., Wahner, A., Kanaya, Y., Yoshino, A., Nishida, S., Kajii, Y., Martinez, M., Kubistin, D., Harder, H., Lelieveld, J., Elste, T., Plass-Dülmer, C., Stange, G., Berresheim, H., and Schurath, U.: HO_x budgets during HOxComp: A case study of HO_x chemistry under NO_x -limited conditions, *J. Geophys. Res.-Atmos.*, 117, D03307, <https://doi.org/10.1029/2011JD017008>, 2012.
- General, S., Pöhler, D., Sihler, H., Bobrowski, N., Frieß, U., Zielcke, J., Horbanski, M., Shepson, P. B., Stirn, B. H., Simpson, W. R., Weber, K., Fischer, C., and Platt, U.: The Heidelberg Airborne Imaging DOAS Instrument (HAIDI) – a novel imaging DOAS device for 2-D and 3-D imaging of trace gases and aerosols, *Atmos. Meas. Tech.*, 7, 3459–3485, <https://doi.org/10.5194/amt-7-3459-2014>, 2014.
- George, M.: Airborne measurement and interpretation of peroxy radical concentrations with a focus on the oxidation mechanisms in the Asian free troposphere, PhD thesis, University of Bremen, <https://doi.org/10.26092/elib/1639>, 2022.
- George, M., Andrés Hernández, M. D., Nenakhov, V., Liu, Y., and Burrows, J. P.: Airborne measurement of peroxy radicals using chemical amplification coupled with cavity ring-down spectroscopy: the PerCEAS instrument, *Atmos. Meas. Tech.*, 13, 2577–2600, <https://doi.org/10.5194/amt-13-2577-2020>, 2020.
- Gerbig, C., Kley, D., Volz-Thomas, A., Kent, J., Dewey, K., and McKenna, D. S.: Fast response resonance fluorescence CO measurements aboard the C-130: Instrument characterisation and measurements made during North Atlantic Regional Experiment 1993, *J. Geophys. Res.*, 101, 29229–29238, 1996.
- Griffith, S. M., Hansen, R. F., Dusanter, S., Michoud, V., Gilman, J. B., Kuster, W. C., Veres, P. R., Graus, M., de Gouw, J. A., Roberts, J., Young, C., Washenfelder, R., Brown, S. S., Thalman, R., Waxman, E., Volkamer, R., Tsai, C., Stutz, J., Flynn, J. H., Grossberg, N., Lefer, B., Alvarez, S. L., Rappenglueck, B., Mielke, L. H., Osthoff, H. D., and Stevens, P. S.: Measurements of Hydroxyl and Hydroperoxy Radicals during CalNexLA: Model Comparisons and Radical Budgets, *J. Geophys. Res.-Atmos.*, 121, 4211–4232, <https://doi.org/10.1002/2015JD024358>, 2016.
- Horstjann, M., Andrés Hernández, M. D., Nenakhov, V., Chrobry, A., and Burrows, J. P.: Peroxy radical detection for airborne atmospheric measurements using absorption spectroscopy of NO_2 , *Atmos. Meas. Tech.*, 7, 1245–1257, <https://doi.org/10.5194/amt-7-1245-2014>, 2014.
- Hüneke, T., Aderhold, O.-A., Bounin, J., Dorf, M., Gentry, E., Grossmann, K., Groß, J.-U., Hoor, P., Jöckel, P., Kenntner, M., Knapp, M., Knecht, M., Lörks, D., Ludmann, S., Matthes, S., Raecke, R., Reichert, M., Weimar, J., Werner, B., Zahn, A., Ziereis, H., and Pfeilsticker, K.: The novel HALO mini-DOAS instrument: inferring trace gas concentrations from airborne UV/visible limb spectroscopy under all skies using the scaling method, *Atmos. Meas. Tech.*, 10, 4209–4234, <https://doi.org/10.5194/amt-10-4209-2017>, 2017.
- Inomata, S., Tanimoto, H., Kameyama, S., Tsunogai, U., Irie, H., Kanaya, Y., and Wang, Z.: Technical Note: Determination of formaldehyde mixing ratios in air with PTR-MS: laboratory experiments and field measurements, *Atmos. Chem. Phys.*, 8, 273–284, <https://doi.org/10.5194/acp-8-273-2008>, 2008.
- Kanaya, Y., Cao, R., Akimoto, H., Fukuda, M., Komazaki, Y., Yokouchi, Y., Koike, M., Tanimoto, H., Takegawa, N., and Kondo, Y.: Urban photochemistry in central Tokyo: 1. Observed and modeled OH and HO_2 radical concentrations during the winter and summer of 2004, *J. Geophys. Res.-Atmos.*, 112, D21312, <https://doi.org/10.1029/2007jd008670>, 2007.
- Kanaya, Y., Fukuda, M., Akimoto, H., Takegawa, N., Komazaki, Y., Yokouchi, Y., Koike, M., and Kondo, Y.: Urban photochemistry in central Tokyo: 2. Rates and regimes of oxidant ($\text{O}_3 + \text{NO}_2$) production, *J. Geophys. Res.*, 113, D06301, <https://doi.org/10.1029/2007JD008671>, 2008.
- Kanaya, Y., Hofzumahaus, A., Dorn, H.-P., Brauers, T., Fuchs, H., Holland, F., Rohrer, F., Bohn, B., Tillmann, R., Wegener, R., Wahner, A., Kajii, Y., Miyamoto, K., Nishida, S., Watanabe, K., Yoshino, A., Kubistin, D., Martinez, M., Rudolf, M., Harder, H., Berresheim, H., Elste, T., Plass-Dülmer, C., Stange, G., Kleffmann, J., Elshorbany, Y., and Schurath, U.: Comparisons of observed and modeled OH and HO_2 concentrations during the ambient measurement period of the HOxComp field campaign, *Atmos. Chem. Phys.*, 12, 2567–2585, <https://doi.org/10.5194/acp-12-2567-2012>, 2012.
- Kartal, D., Andrés-Hernández, M. D., Reichert, L., Schlager, H., and Burrows, J. P.: Technical Note: Characterisation of a DUALER instrument for the airborne measurement of peroxy radicals during AMMA 2006, *Atmos. Chem. Phys.*, 10, 3047–3062, <https://doi.org/10.5194/acp-10-3047-2010>, 2010.
- Kleinman, L., Lee, Y.-N., Springston, S. R., Lee, J. H., Nunnermacker, L., Weinstein-Lloyd, J., Zhou, X., and Newman, L.: Peroxy

- radical concentration and ozone formation rate at a rural site in southeastern United States, *J. Geophys. Res.*, 100, 7263–7273, 1995.
- Kluge, F., Hüneke, T., Knecht, M., Lichtenstern, M., Rotermund, M., Schlager, H., Schreiner, B., and Pfeilsticker, K.: Profiling of formaldehyde, glyoxal, methylglyoxal, and CO over the Amazon: normalized excess mixing ratios and related emission factors in biomass burning plumes, *Atmos. Chem. Phys.*, 20, 12363–12389, <https://doi.org/10.5194/acp-20-12363-2020>, 2020.
- Lew, M. M., Rickly, P. S., Bottorff, B. P., Reidy, E., Sklaveniti, S., Léonardis, T., Locoge, N., Dusanter, S., Kundu, S., Wood, E., and Stevens, P. S.: OH and HO₂ radical chemistry in a midlatitude forest: measurements and model comparisons, *Atmos. Chem. Phys.*, 20, 9209–9230, <https://doi.org/10.5194/acp-20-9209-2020>, 2020.
- Lu, K. D., Rohrer, F., Holland, F., Fuchs, H., Bohn, B., Brauers, T., Chang, C. C., Häseler, R., Hu, M., Kita, K., Kondo, Y., Li, X., Lou, S. R., Nehr, S., Shao, M., Zeng, L. M., Wahner, A., Zhang, Y. H., and Hofzumahaus, A.: Observation and modelling of OH and HO₂ concentrations in the Pearl River Delta 2006: a missing OH source in a VOC rich atmosphere, *Atmos. Chem. Phys.*, 12, 1541–1569, <https://doi.org/10.5194/acp-12-1541-2012>, 2012.
- Lu, K. D., Hofzumahaus, A., Holland, F., Bohn, B., Brauers, T., Fuchs, H., Hu, M., Häseler, R., Kita, K., Kondo, Y., Li, X., Lou, S. R., Oebel, A., Shao, M., Zeng, L. M., Wahner, A., Zhu, T., Zhang, Y. H., and Rohrer, F.: Missing OH source in a suburban environment near Beijing: observed and modelled OH and HO₂ concentrations in summer 2006, *Atmos. Chem. Phys.*, 13, 1057–1080, <https://doi.org/10.5194/acp-13-1057-2013>, 2013.
- Mallaun, C., Giez, A., and Baumann, R.: Calibration of 3-D wind measurements on a single-engine research aircraft, *Atmos. Meas. Tech.*, 8, 3177–3196, <https://doi.org/10.5194/amt-8-3177-2015>, 2015.
- Mao, J., Jacob, D. J., Evans, M. J., Olson, J. R., Ren, X., Brune, W. H., Clair, J. M. St., Crounse, J. D., Spencer, K. M., Beaver, M. R., Wennberg, P. O., Cubison, M. J., Jimenez, J. L., Fried, A., Weibring, P., Walega, J. G., Hall, S. R., Weinheimer, A. J., Cohen, R. C., Chen, G., Crawford, J. H., McNaughton, C., Clarke, A. D., Jaeglé, L., Fisher, J. A., Yantosca, R. M., Le Sager, P., and Carouge, C.: Chemistry of hydrogen oxide radicals (HOx) in the Arctic troposphere in spring, *Atmos. Chem. Phys.*, 10, 5823–5838, <https://doi.org/10.5194/acp-10-5823-2010>, 2010.
- Martinez, M., Harder, H., Kovacs, T. A., Simpas, J. B., Bassis, J., Leshner, R., Brune, W. H., Frost, G. J., Williams, E. J., Stroud, C. A., Jobson, B. T., Roberts, J. M., Hall, S. R., Shetter, R. E., Wert, B., Fried, A., Alicke, B., Stutz, J., Young, V. L., White, A. B., and Zamora, R. J.: OH and HO₂ concentrations, sources, and loss rates during the Southern Oxidants Study in Nashville, Tennessee, summer 1999, *J. Geophys. Res.-Atmos.*, 108, 4617, <https://doi.org/10.1029/2003jd003551>, 2003.
- Mihelcic, D., Holland, F., Hofzumahaus, A., Hoppe, L., Konrad, S., Müsgen, P., Pätz, H.-W., Schäfer, H.-J., Schmitz, T., Volz-Thomas, A., Bächmann, K., Schlowski, S., Platt, U., Geyer, A., Alicke, B., and Moortgat, G. K.: Peroxy radicals during BERLIOZ at Pabstthum: Measurements, radical budgets and ozone production, *J. Geophys. Res.-Atmos.*, 108, 8254, <https://doi.org/10.1029/2001JD001014>, 2003.
- Mihele, C. M. and Hastie, D. R.: The sensitivity of the radical amplifier to ambient water vapour, *Geophys. Res. Lett.*, 25, 1911–1913, <https://doi.org/10.1029/98GL01432>, 1998.
- Mihele, C. M., Mozurkewich, M., and Hastie, D. R.: Radical loss in a chain reaction of CO and NO in the presence of water: Implications for the radical amplifier and atmospheric chemistry, *Int. J. Chem. Kinet.*, 31, 145–152, [https://doi.org/10.1002/\(SICI\)1097-4601\(1999\)31:2<145::AID-KIN7>3.0.CO;2-M](https://doi.org/10.1002/(SICI)1097-4601(1999)31:2<145::AID-KIN7>3.0.CO;2-M), 1999.
- Parrish, D. D., Trainer, M., Williams, E. J., Fahey, D. W., Hobler, G., Eubank, C. S., Liu, S. C., Murphy, P. C., Albritton, D. L., and Fehsenfeld, F. C.: Measurements of the NO_x-O₃ photostationary state at Niwot Ridge, Colorado, *J. Geophys. Res.*, 91, 5361–5370, 1986.
- re3data.org: HALO database; editing status 2021-11-17, re3data.org – Registry of Research Data Repositories [data set], <https://doi.org/10.17616/R39Q0T>, 2022.
- Reichert, L., Andrés Hernández, M. D., Stöbener, D., Burkert, J., and Burrows, J. P.: Investigation of the effect of water complexes in the determination of peroxy radical ambient concentrations: implications for the atmosphere, *J. Geophys. Res.*, 108, 4017–4032, <https://doi.org/10.1029/2002JD002152>, 2003.
- Ren, X., Harder, H., Martinez, M., Leshner, R. L., Oligier, A., Shirley, T., Adams, J., Simpas, J. B., and Brune, W. H.: HOx concentrations and OH reactivity observations in New York City during PMTACS-NY2001, *Atmos. Environ.*, 37, 3627–3637, 2003.
- Ren, X., van Duin, D., Cazorla, M., Chen, S., Mao, J., Zhang, L., Brune, W. H., Flynn, J. H., Grossberg, N., Lefer, B. L., Rappenglück, B., Wong, K. W., Tsai, C., Stutz, J., Dibb, J. E., Thomas Jobson, B., Luke, W. T., and Kelley, P.: Atmospheric oxidation chemistry and ozone production: Results from SHARP 2009 in Houston, Texas, *J. Geophys. Res.*, 118, 5770–5780, <https://doi.org/10.1002/jgrd.50342>, 2013.
- Ridley, B. A., Madronich, S., Chatfield, R. B., Walega, J. G., and Shetter, R. E.: Measurements and model simulations of the photostationary state during the Mauna Loa observatory photochemistry experiment: Implications for radical concentrations and ozone production and loss rates, *J. Geophys. Res.*, 97, 10375–10388, 1992.
- Rotermund, M. K., Bense, V., Chipperfield, M. P., Engel, A., Groß, J.-U., Hoor, P., Hüneke, T., Keber, T., Kluge, F., Schreiner, B., Schuck, T., Vogel, B., Zahn, A., and Pfeilsticker, K.: Organic and inorganic bromine measurements around the extratropical tropopause and lowermost stratosphere: insights into the transport pathways and total bromine, *Atmos. Chem. Phys.*, 21, 15375–15407, <https://doi.org/10.5194/acp-21-15375-2021>, 2021.
- Schumann, U.: Measurement and model data comparisons for the HALO-FAAM formation flight during EMeRGe on 17 July 2017, Zenodo [data set], <https://doi.org/10.5281/zenodo.4427965>, 2020.
- Stohl, A. and Seibert, P.: Accuracy of trajectories as determined from the conservation of meteorological tracers, *Q. J. Roy. Meteor. Soc.*, 124, 1465–1484, <https://doi.org/10.1256/smsqj.54906>, 1998.
- Stohl, A., Wotawa, G., Seibert, P., and Kromp-Kolb, H.: Interpolation Errors in Wind Fields as a Function of Spatial and Temporal Resolution and Their Impact on Different Types of Kinematic Trajectories, *J. Appl. Me-*

- teorol., 34, 2149–2165, [https://doi.org/10.1175/1520-0450\(1995\)034<2149:IEIWFA>2.0.CO;2](https://doi.org/10.1175/1520-0450(1995)034<2149:IEIWFA>2.0.CO;2), 1995.
- Stutz, J., Werner, B., Spolaor, M., Scalone, L., Festa, J., Tsai, C., Cheung, R., Colosimo, S. F., Tricoli, U., Raecke, R., Hossaini, R., Chipperfield, M. P., Feng, W., Gao, R.-S., Hints, E. J., Elkins, J. W., Moore, F. L., Daube, B., Pittman, J., Wofsy, S., and Pfeilsticker, K.: A new Differential Optical Absorption Spectroscopy instrument to study atmospheric chemistry from a high-altitude unmanned aircraft, *Atmos. Meas. Tech.*, 10, 1017–1042, <https://doi.org/10.5194/amt-10-1017-2017>, 2017.
- Tan, D., Faloon, I., Simpas, J. B., Brune, W., Olson, J., Crawford, J., Avery, M., Sachse, G., Vay, S., Sandholm, S., Guan, H.-W., Vaughn, T., Mastromarino, J., Heikes, B., Snow, J., Podolske, J., and Singh, H.: OH and HO₂ in the tropical Pacific: Results from PEMTropics B, *J. Geophys. Res.*, 106, 32667–32681, 2001.
- Tan, Z., Fuchs, H., Lu, K., Hofzumahaus, A., Bohn, B., Broch, S., Dong, H., Gomm, S., Häseler, R., He, L., Holland, F., Li, X., Liu, Y., Lu, S., Rohrer, F., Shao, M., Wang, B., Wang, M., Wu, Y., Zeng, L., Zhang, Y., Wahner, A., and Zhang, Y.: Radical chemistry at a rural site (Wangdu) in the North China Plain: observation and model calculations of OH, HO₂ and RO₂ radicals, *Atmos. Chem. Phys.*, 17, 663–690, <https://doi.org/10.5194/acp-17-663-2017>, 2017.
- Tan, Z., Rohrer, F., Lu, K., Ma, X., Bohn, B., Broch, S., Dong, H., Fuchs, H., Gkatzelis, G. I., Hofzumahaus, A., Holland, F., Li, X., Liu, Y., Liu, Y., Novelli, A., Shao, M., Wang, H., Wu, Y., Zeng, L., Hu, M., Kiendler-Scharr, A., Wahner, A., and Zhang, Y.: Wintertime photochemistry in Beijing: observations of RO_x radical concentrations in the North China Plain during the BEST-ONE campaign, *Atmos. Chem. Phys.*, 18, 12391–12411, <https://doi.org/10.5194/acp-18-12391-2018>, 2018.
- Tan, Z., Lu, K., Hofzumahaus, A., Fuchs, H., Bohn, B., Holland, F., Liu, Y., Rohrer, F., Shao, M., Sun, K., Wu, Y., Zeng, L., Zhang, Y., Zou, Q., Kiendler-Scharr, A., Wahner, A., and Zhang, Y.: Experimental budgets of OH, HO₂, and RO₂ radicals and implications for ozone formation in the Pearl River Delta in China 2014, *Atmos. Chem. Phys.*, 19, 7129–7150, <https://doi.org/10.5194/acp-19-7129-2019>, 2019.
- Volz-Thomas, A., Pätz, H.-W., Houben, N., Konrad, S., Mihelcic, D., Klüpfel, T., and Perner, D.: Inorganic trace gases and peroxy radicals during BERLIOZ at Pabstthum: An investigation of the photostationary state of NO_x and O₃, *J. Geophys. Res.*, 108, PHO 4-1, <https://doi.org/10.1029/2001JD001255>, 2003.
- Whalley, L. K., Stone, D., Dunmore, R., Hamilton, J., Hopkins, J. R., Lee, J. D., Lewis, A. C., Williams, P., Kleffmann, J., Laufs, S., Woodward-Massey, R., and Heard, D. E.: Understanding in situ ozone production in the summertime through radical observations and modelling studies during the Clean air for London project (ClearLo), *Atmos. Chem. Phys.*, 18, 2547–2571, <https://doi.org/10.5194/acp-18-2547-2018>, 2018.
- Whalley, L. K., Slater, E. J., Woodward-Massey, R., Ye, C., Lee, J. D., Squires, F., Hopkins, J. R., Dunmore, R. E., Shaw, M., Hamilton, J. F., Lewis, A. C., Mehra, A., Worrall, S. D., Bacak, A., Bannan, T. J., Coe, H., Percival, C. J., Ouyang, B., Jones, R. L., Crilley, L. R., Kramer, L. J., Bloss, W. J., Vu, T., Kotthaus, S., Grimmond, S., Sun, Y., Xu, W., Yue, S., Ren, L., Acton, W. J. F., Hewitt, C. N., Wang, X., Fu, P., and Heard, D. E.: Evaluating the sensitivity of radical chemistry and ozone formation to ambient VOCs and NO_x in Beijing, *Atmos. Chem. Phys.*, 21, 2125–2147, <https://doi.org/10.5194/acp-21-2125-2021>, 2021.
- Zahn, A., Weppner, J., Widmann, H., Schlote-Holubek, K., Burger, B., Kühner, T., and Franke, H.: A fast and precise chemiluminescence ozone detector for eddy flux and airborne application, *Atmos. Meas. Tech.*, 5, 363–375, <https://doi.org/10.5194/amt-5-363-2012>, 2012.
- Zarzana, K. J., Min, K.-E., Washenfelder, R. A., Kaiser, J., Krawiec-Thayer, M., Peischl, J., Neuman, J. A., Nowak, J. B., Wagner, N. L., Dubè, W. P., St. Clair, J. M., Wolfe, G. M., Hanisco, T. F., Keutsch, F. N., Ryerson, T. B., and Brown, S. S.: Emissions of Glyoxal and Other Carbonyl Compounds from Agricultural Biomass Burning Plumes Sampled by Aircraft, *Environ. Sci. Technol.*, 51, 11761–11770, <https://doi.org/10.1021/acs.est.7b03517>, 2017.
- Ziereis, H., Minikin, A., Schlager, H., Gayet, J. F., Auriol, F., Stock, P., Baehr, J., Petzold, A., Schumann, U., Weinheimer, A., Ridley, B., and Ström, J.: Uptake of reactive nitrogen on cirrus cloud particles during INCA, *Geophys. Res. Lett.*, 31, L05115, <https://doi.org/10.1029/2003GL018794>, 2004.